The cordierite-bearing anatectic rocks of the Higher Himalayan Crystallines (eastern Nepal): low-pressure anatexis, melt-productivity, melt loss and the preservation of cordierite.

THE CORDIERITE-BEARING ANATECTIC ROCKS OF THE HIGHER HIMALAYAN CRYSTALLINES (EASTERN NEPAL): LOW-PRESSURE ANATEXIS, MELT-PRODUCTIVITY, MELT LOSS AND THE PRESERVATION OF CORDIERITE

Chiara Groppo[1*], Franco Rolfo[1,2], Pietro Mosca[2]

1 - Department of Earth Sciences, University of Torino, via Valperga Caluso 35, I-10125, Torino, Italy
2 - IGG – CNR, Via Valperga Caluso 35, I-10125, Torino, Italy

[*] **Corresponding author:**
Chiara Groppo
Phone: +39 011 6705106
Fax: +39 011 6705128
e-mail: chiara.groppo@unito.it

Abstract

Cordierite-bearing anatectic rocks inform our understanding of low-pressure anatectic processes in the continental crust. This paper focuses on cordierite-bearing lithologies occurring at the upper structural levels of the Higher Himalayan Crystallines (eastern Nepal Himalaya). Three cordierite-bearing gneisses from different geological transects (from mount Everest to Kangchenjunga) have been studied, in which cordierite is spectacularly well preserved. The three samples differ in terms of bulk composition likely reflecting different sedimentary protoliths, though they all consist of quartz, alkali feldspar, plagioclase, biotite, cordierite and sillimanite in different modal percentages.

Analysis of the microstructures related to melt production and/or melt consumption allows the distinction to be made between peritectic and cotectic cordierite. The melt productivity of different prograde assemblages (from two-micas metapelite/metagreywacke to biotite-metapelite) has been investigated at low pressure conditions, evaluating the effects of muscovite vs. biotite de-hydration melting on both mineral assemblages and microstructures. The results of the thermodynamic modelling suggest that the mode and type of the micaceous minerals in the prograde assemblage is a very important parameter controlling the melt productivity at low pressure conditions, the two-mica protoliths being significantly more fertile at any given temperature than biotite gneisses over the same temperature interval. Furthermore, the cordierite preservation is promoted by melt crystallization at a dry *solidus* and by exhumation along *P*-*T* paths with a peculiar d*P*/d*T* slope of about 15-18 bar °C^{-1}. Overall, our results provide a key for the interpretation of cordierite petrogenesis in migmatites from any low-*P* regional anatectic terrane.

The cordierite-bearing migmatites may well represent the source rocks for the Miocene andalusite-bearing leucogranites occurring at the upper structural levels of the Himalayan belt, and low-*P* isobaric heating rather than decompression melting may be the triggering process of this peculiar peraluminous magmatism.

Key words: cordierite-bearing anatectic rocks, low-pressure anatexis, *P*-*T* pseudosections, Higher Himalayan Crystallines, Himalaya

INTRODUCTION

Cordierite-bearing anatectic rocks are characteristic of partial melting at low pressure conditions (e.g. Spear *et al.*, 1999). Microstructural and petrological study of cordierite-bearing rocks is thus relevant, besides contact metamorphism, for the understanding of regional metamorphic terranes where partial melting occurred at remarkably shallow-crustal pressures. Furthermore, cordierite is potentially a powerful mineral monitor of fluid conditions during high grade metamorphism (Vry *et al*., 1990; Visser *et al*., 1994; Carrington & Harley, 1996; Harley & Carrington, 2001; Thompson *et al*., 2001; Harley *et al*., 2002; Bertoldi *et al*., 2004). Hence, the study of *P-T* conditions at which cordierite grows, combined with the information on the activities and compositions of fluids, could provide useful constraints for the understanding of low pressure anatectic processes.

Experimental studies (e.g. Vielzeuf & Montel, 1994; Carrington & Harley, 1995; Stevens *et al*., 1995, 1997; Montel & Vielzeuf, 1997; Buick *et al*., 2004; Grant, 2004; Spicer *et al*., 2004) and phase equilibria modelling (e.g. Waters, 1988; Harley, 1994; Carrington & Harley, 1995; Fitzsimons, 1996; Buick *et al*., 1998; Johnson *et al*., 2001) focusing on partial melting of pelitic and/or psammitic protoliths at low pressure (i.e. $P \leq 5$ kbar) suggest that cordierite can be formed, at supra-*solidus* conditions, by two significantly different processes. First, cordierite may be a peritectic phase derived from incongruent melting reactions at increasing temperature, with or without significant decompression, for example through the dehydration melting reaction Qtz + Sil + Bt → Kfs + Crd + L. Alternatively, cordierite may be the product of "magmatic cotectic" crystallization at decreasing temperature (± decompression), for example through the reaction L → Qtz + Kfs + Crd + V (e.g. Clarke, 1995; Grant, 2004). These two cordierite-forming processes yield significantly different microstructures (e.g. Pereira & Bea, 1994; Clarke, 1995; Barbey *et al*., 1999; Johnson *et al*., 2001; Grant, 2004), whose correct interpretation could bear important information about the *P-T* evolution of the anatectic rocks. A peritectic growth of cordierite (i.e. at increasing *T*) is suggested by the occurrence of large cordierite poikiloblasts with rounded and corroded inclusions of those minerals that are reactants in the incongruent melting reaction, typically quartz, sillimanite, biotite and/or plagioclase (Blümel & Schreyer, 1977; Barbey *et al*., 1999). In this case, quartz, sillimanite and biotite are never in mutual contact, but are always separated by cordierite, and in most cases one of these reactants (typically sillimanite) does not occur outside the cordierite poikiloblasts (e.g. Sawyer, 2008). Cotectic cordierite growth during melt crystallization (i.e. at decreasing *T*) typically occurs in the leucosomes of migmatites and in granites as subhedral to euhedral prismatic crystals showing equilibrium relationships with quartz and feldspar (e.g. Clarke, 1995; Barbey *et al*., 1999; Johnson *et al*., 2001) and with only few inclusions.

Thanks to the recent advances in the thermodynamic datasets (e.g. Holland & Powell, 2001; White *et al*., 2001, 2007; White & Powell, 2002) it is now possible to reliably model the *P-T* evolution of high-*T*, low-*P* metamorphic terranes taking in account the production of melt at increasing temperature (e.g. White *et al*., 2001, 2003; Johnson *et al*., 2008), the influence of melt production on the mineral assemblage evolution following the peak of metamorphism (e.g. Brown, 2002; Kelsey *et al*., 2003; White & Powell, 2011), and the effect of possible melt loss at certain metamorphic stages (e.g. White & Powell, 2002; Clarke *et al*., 2007; Halpin *et al*., 2007). Therefore, the *P-T* pseudosection approach has become an increasingly used and often invaluable tool to investigate the metamorphic history of anatectic rocks, providing that a detailed petrographic interpretation of the key microstructures relevant to the melt-producing and melt-consuming

reactions is given (e.g. White *et al*., 2003; Johnson *et al*., 2004; Sajeev *et al*., 2006; Groppo *et al*., 2010, 2012).

With this purpose in mind, we focus on the cordierite-bearing anatectic lithologies occurring at the upper structural levels of the Higher Himalayan Crystallines in eastern Himalaya. Detailed petrographic characterization of three samples from different geological transects in eastern Nepal (from Everest to Kangchenjunga regions) is used to analyze the relevant microstructures related to melt production and/or melt consumption and to distinguish between peritectic and cotectic cordierite. The *P-T* pseudosection approach is subsequently used to constrain the *P-T* evolution of these cordierite-bearing samples with the main aims of: (i) investigating the melt productivity, at low-*P* conditions, of different prograde assemblages (from two-micas metapelite/metagreywacke to biotite-metapelite), evaluating the effects of muscovite vs. biotite de-hydration melting on both mineral assemblages and microstructures, and (ii) understanding why samples show a lack of retrograde hydration, resulting in the preservation of cordierite crystals.

GEOLOGICAL SETTING

Cordierite-bearing assemblages in the Higher Himalayan Crystallines

The Himalayan belt comprises few lithotectonic units extending throughout the length of the chain and separated by major north-dipping tectonic contacts (Fig. 1). In the north, the medium- to high-grade Higher Himalayan Crystalline (HHC), intruded in the upper structural levels by leucogranites, is overlain by the Tethys Sedimentary Sequence (TSS) along the South Tibetan Detachment System (STDS). The south-verging Main Central Thrust Zone (MCTZ) juxtaposes the HHC over the low-grade Lesser Himalayan Sequence (LHS). Moving to the south, the Lesser Himalayan Sequence structurally overlie along the Main Boundary Thrust the Sub-Himalayan molasse, in turn deformed by the Main Frontal Thrust system (e.g. Le Fort, 1975).

Generally speaking, there is a marked difference in the metamorphic evolution of the Himalayan crystalline nappes along strike, the western ones lacking the high-temperature overprinting widespread in the eastern ones (Lombardo & Rolfo, 2000). This feature also affects the *P-T* history of the few high-pressure lithologies found so far in the western (Lombardo *et al*., 2000) and eastern (Groppo *et al*., 2007) side of the chain. However, partial melting is widely documented in the HHC, a high-grade, several-km-thick lithotectonic unit (e.g. Goscombe *et al*., 2006; Searle *et al*., 2008). In the lower structural levels of the HHC, anatexis developed at medium to high-*P* (i.e. 8-12 kbar: e.g. Streule *et al*., 2010; Groppo *et al*., 2012) and is recorded in kyanite-bearing granulites (regionally known in eastern Nepal as Barun gneiss and Jannu-Kangchenjunga gneiss: e.g. Bordet, 1961; Lombardo *et al*., 1993; Goscombe *et al*., 2006), characterized by the typical assemblage biotite + quartz + alkali feldspar + plagioclase + garnet + sillimanite ± kyanite. Toward the upper structural levels of the HHC, peak-pressure significantly decreases to 4-5 kbar, as revealed by the widespread occurrence of cordierite-bearing and kyanite-free gneisses (e.g. Pognante & Benna, 1993; Goscombe & Hand, 2000; Streule *et al*., 2010; Mosca *et al*., 2011).

In the eastern Nepal Himalaya, the occurrence of cordierite-bearing rocks in the HHC is well known since the pioneering studies of Lombard (1958) and Bordet (1961). Cordierite-bearing anatectic gneisses and migmatites are described by Lombardo *et al*. (1993) and Pognante & Benna (1993) from the Everest and Makalu regions (upper Khumbu and Barun valleys): these authors suggested that cordierite + sillimanite + biotite ± garnet assemblages characterize the medium to upper structural levels of the HHC, regionally known as Namche Migmatite Orthogneiss and Black

gneiss. The same assemblages are also reported by Streule *et al*. (2010) along the upper Barun valley: these authors further specify that at the uppermost structural levels of the HHC, cordierite is prominent and garnet is often absent. In addition, cordierite-bearing two-mica granitic bodies and dykes, locally containing andalusite, are hosted in the upper HHC (e.g. Visonà & Lombardo, 2002; Searle *et al*., 2010; Streule *et al*., 2010; Visonà *et al*., 2012). In these lithologies, cordierite occurs in two different microstructural domains: (i) as variably thick coronas partially replacing garnet and/or sillimanite, and (ii) as large euhedral crystals within leucosomes, both concordant and discordant with respect to the main foliation (e.g. Pognante & Benna, 1993; Goscombe & Hand, 2000; Visonà & Lombardo, 2002; Borghi *et al*., 2003; Imayama *et al*., 2010; Streule *et al*., 2010).

In comparison with the numerous reports of cordierite-bearing rocks in the HHC, studies focusing on the reconstruction of the *P-T* evolution of such low pressure anatectic rocks are scarce. In the HHC of eastern Nepal, cordierite growth is attributed to a migmatization event at 600-700°C, 2-4 kbar by Pognante & Benna (1993), on the base of conventional thermobarometry. Higher peak *T* and *P* (700-800°C, 4-6 kbar) have been obtained on similar rocks using the THERMOCALC "Average *PT*" method (e.g. Goscombe & Hand, 2000; Imayama *et al*., 2010; Streule *et al*., 2010). The *P-T* pseudosection approach was applied by Streule *et al*. (2010) on a cordierite-bearing leucogranite from the upper Barun valley, interpreted as documenting the final melt crystallization at about 700°C, 3 kbar. To our knowledge, the pseudosection approach has not yet been used to constrain the *P-T* evolution of cordierite-bearing rocks in the Himalaya of eastern Nepal. Regardless of the method used to constrain the *P-T* path of these rocks, the frequent occurrence of cordierite coronas replacing garnet has been commonly interpreted as the product of nearly-isothermal decompression following rapid exhumation. However, the main cordierite-producing and garnet-consuming reaction (i.e. Bt + Grt + Als = Crd + Kfs + L) for the metapelitic system has a positive, although moderate, slope (e.g. Spear *et al*., 1999; White *et al*., 2001, 2007; Wei & Powell, 2004), thus implying that cordierite growth may occur either during decompression or during heating.

Sample locations

Three cordierite-bearing gneisses (samples 09-29, 07-26 and 05-17) from different geological transects in Eastern Nepal (Everest, Makalu and Kangchenjunga regions) and from medium to upper structural levels of the HHC (Fig. 1), have been studied in detail. From east to west, sample 09-29 was collected at Phole, Ghunsa Khola valley (3200 m a.s.l.), in the Kangchenjunga region of far-east Nepal (Mosca *et al*., 2011), and is the structurally lowermost sample. It is a medium-grained biotite + sillimanite ± garnet migmatitic gneiss with cm-thick leucosomes concordant with the main foliation (Fig. 2a). Samples 07-26 and 05-17 were collected at significantly higher structural levels. Sample 07-26 comes from a wallrock on the western side of the Barun Glacier, above the Makalu Base Camp (5130 m a.s.l.), whereas sample 05-17 was collected at Lunag, along the upper Bhote Khosi Valley on the eastern side of the Nangpa glacier (about 5100 m a.s.l.). Both samples are fine-grained dark biotite + sillimanite gneiss. Sample 07-26 is spotted and is characterized by plurimillimetric white nodules apparently enveloped by the main foliation, and shows thin and discontinuous leucosomes (Fig. 2b). Sample 05-17 has a massive appearance and is crosscut by decimeter-thick granitic dykes discordant with respect to the main foliation (Fig. 2c).

PETROGRAPHY AND MINERAL CHEMISTRY

The samples have different bulk composition (Fig. S1) though they all consist of quartz, alkali-feldspar, plagioclase, biotite, cordierite and sillimanite with different modes. Given the strongly heterogeneous fabric of the samples, the modal percentages of each mineral have been obtained from qualitative major elements X-ray maps extended over the whole thin sections (Fig. 3). The main textural differences relate to: (i) the modal proportion of leucocratic vs. mesocratic domains: samples 09-29 and 07-26 are dominated by leucocratic domains (Qtz + Kfs + Pl = 71 vol% and 60 vol%, respectively), whereas in sample 05-17 the mesocratic domains prevail (Bt + Crd + Sil = 61 vol%); (ii) the relative proportion between plagioclase and alkali feldspar, which varies from 1:10 (sample 07-26), to 1:1 (sample 09-29) and to 6:1 (sample 05-17). Microstructural features are illustrated in Figs 3, 4 & S3. Details on the methods used to obtain the micro-XRF maps and the mineral chemistry are given in the Appendix S1.

Sample 09-29

Microstructure

Sample 09-29 is an anatectic gneiss consisting of quartz (36 vol%), alkali feldspar (19 vol%), plagioclase (16 vol%), cordierite (16 vol%), biotite (9 vol%) sillimanite (4 vol%) and minor garnet and ilmenite. The gneissic structure is defined by coarse-grained leucocratic quartzo-feldspathic domains alternated with mesocratic domains mainly consisting of oriented biotite and sillimanite overgrown by cordierite and defining the main, locally folded, foliation (Figs 3 & 4a).

Alkali feldspar forms coarse-grained poikiloblasts in the leucocratic domains (Fig. 3), with abundant inclusions of biotite (Bt_1), rounded plagioclase (Pl_1) and quartz, and very minor sillimanite (Sil_1) and cordierite (Fig. 4c). It is only locally replaced at its rim by plagioclase (Pl_2) + sillimanite (Sil_2) patches (Fig. S3b) or by myrmeckitic intergrowths of plagioclase + quartz. Plagioclase (Pl_1) occurs in two different microstructural positions: as small rounded inclusions within poikiloblastic alkali feldspar (Fig. 4c) and as large crystals in the leucocratic quartzo-feldspathic domains. In both cases Pl_1 is antiperthitic, showing large (up to 50 μm) alkali feldspar exsolution lamellae.

Cordierite occurs in the mesocratic domains (Fig. 3) and, more rarely, in the leucocratic layers. In the first case, it forms large porphyroblasts (several millimetres in length) that are elongated in the plane of the main foliation and mimetically overgrow the biotite (Bt_1) + sillimanite (Sil_1) layers (Fig. 4a,b). Sil_1 and Bt_1 never occur in mutual contact, as they are always separated by cordierite. More rarely, cordierite also occurs in the leucocratic domains at the contact with the mesocratic layers, where it forms subhedral grains with rare quartz and biotite (Bt_1) inclusions (Fig. 4a). Garnet is a relict phase, replaced by either thick coronas of cordierite (in the mesocratic domains; Fig. 4b) or discontinuous coronas of plagioclase (Pl_2) (in the leucocratic domains; Fig. 4a): it is locally crowded with very small dark and isotropic rounded inclusions. Most biotite (Bt_1) and sillimanite (Sil_1) in this sample, defining the main foliation, is enveloped by either cordierite or, more rarely, alkali feldspar poikiloblasts (Fig. 3). A late biotite generation is locally observed at the contact between Bt_1 and alkali feldspar, as fine-grained symplectitic intergrowths of Bt_2 and quartz (Fig. S3c).

Mineral chemistry

Biotite – Bt_1 is characterized by relatively high Ti contents, ranging from 0.25 to 0.32 a.p.f.u. (on the basis of 11 oxygens) and by a homogeneous X_{Mg}, in the range 0.34-0.36. The Al^{VI} content

decreases with increasing Ti, in the range 0.15-0.27 a.p.f.u. Bt_1 included in alkali feldspar poikiloblasts has, on average, a lower Ti content and a slightly higher Al^{VI} than Bt_1 in the mesocratic domains (Fig. 5a). Locally, a significant decrease in Ti contents to 0.20 a.p.f.u. (counterbalanced by an increase in both X_{Mg} and Al^{VI}, up to 0.38 and 0.36 a.p.f.u., respectively) has been observed at the rim of Bt_1. Bt_2 has relatively low Ti contents (0.19-0.21 a.p.f.u.) and high X_{Mg} (0.36-0.37) and Al^{VI} (0.31-0.37 a.p.f.u.) (Fig. 5a).

Plagioclase – Pl_1 inclusions within alkali feldspar show the larger variability in composition, with X_{An}=0.28-0.32, whereas the large antiperthite crystals in the leucocratic domains have X_{An}=0.31-0.32. This large antiperthitic feldspar shows a homogeneous rim (i.e. without K-feldspar exsolutions) clearly corroding biotite or alkali feldspar poikiloblasts and characterized by higher anorthite contents (X_{An}=0.33), similar to the X_{An} of Pl_2 (X_{An}=0.33-0.34) (Fig. 5c). Finally, a thin albitic rim is generally observed at the interface between rounded inclusions of Pl_1 and poikiloblastic alkali feldspar.

Cordierite – The poikiloblastic cordierite in the mesocratic domains is quite homogeneous in composition, with X_{Mg} ranging from 0.54 to 0.51, the lower X_{Mg} values generally toward the rims. The subhedral cordierite crystals in the leucocratic domains has a slightly but significantly lower X_{Mg} values, in the range 0.49-0.50. Plotted in the (Si+Al) vs. (Mg+Mn+Fe) diagram (Bertoldi *et al*., 2004) (Fig. 5b), both cordierite types lie along the $^{Ch}Na^{+IV}(Mg^{2+},Fe^{2+}) = {}^{Ch}\square{}^{+IV}Al^{3+}$ exchange vector, thus suggesting that cordierite does not contain Be and Li. Micro-Raman spectra on both cordierite varieties in *aa* geometry as described by Kaindl *et al*. (2006) do not show the 1383 cm^{-1} peak (Fig. S2) which is diagnostic for the presence of CO_2 (e.g. Kolesov & Geiger, 2000; Kaindl *et al*., 2006).

Alkali feldspar – It is generally perthitic and has a X_{Ab} in the range 0.11-0.15.

Garnet – Is a relict phase partially replaced either by cordierite or by plagioclase (Pl_2). X_{Ca} is about 0.03; a slight increase in X_{Mn} is observed toward the rim, counterbalanced by a decrease in X_{Mg} (X_{Mn}=0.06-0.07; X_{Mg}=0.12-0.10).

Sample 07-26

Microstructure

Sample 07-26 is a medium-grained biotitic gneiss with a nodular appearance, with alkali feldspar (30 vol%), quartz (27 vol%), cordierite (17 vol%), biotite (15 vol%), sillimanite (8 vol%) and minor plagioclase (3 vol%), very small garnet relicts and accessory ilmenite and apatite. The mm-spaced and discontinuous foliation is defined by biotite and wraps around millimetric nodules of cordierite crowded of fine-grained sillimanite (Figs 3 & 4d,). Cordierite nodules generally show a flattened lozenge shape, with sillimanite inclusions (Sil_1) locally concentrated along the two diagonals of the lozenge (Figs 4d & S3d).

Alkali feldspar forms large poikiloblasts with abundant inclusions of biotite (Bt_1), sillimanite (Sil_1), cordierite, rounded plagioclase (Pl_1) and quartz (Fig. S3e). Bt_1 included in alkali feldspar is aligned parallel to the main foliation (Figs 4e & S3e). Plagioclase is rare and mainly occurs as large Pl_2 patches (Figs 3, 4g & S3f) partially replacing alkali feldspar, Bt_1 and garnet. Small and idioblastic biotite flakes (Bt_2) are often present in these Pl_2 patches (Fig. S3f), as well as fine-grained sillimanite (Sil_2) (Fig. 4g).

Mineral chemistry

Biotite – Bt_1 has Ti in the range 0.14-0.28 a.p.f.u., inversely proportional to the Al^{VI} (0.25-0.44 a.p.f.u.); X_{Mg} is more homogeneous, in the range 0.31-0.36. A local decrease in Ti, counterbalanced by an increase in both X_{Mg} and Al^{VI} is observed toward Bt_1 rims (Fig. 5a). The rare Bt_2 has a composition significantly different from that of Bt_1, being lower in Ti (0.12-0.19 a.p.f.u.) and higher in Al^{VI} (0.44-0.57 a.p.f.u.), whereas X_{Mg} is in the range 0.32-0.33 (Fig. 5a).

Plagioclase –Pl_1 has a relatively low X_{An} content, in the range 0.26-0.29, significantly lower than the X_{An} of the large Pl_2 patches (X_{An}=0.29-0.35) (Fig. 5c). The highest anorthite contents have been observed in the Pl_2 patches corroding garnet relicts.

Cordierite – Cordierite nodules are homogeneous, with X_{Mg} ranging from 0.48 to 0.50. No significant variations have been observed for the cordierite inclusions within alkali feldspar poikiloblasts. Cordierite lies along the $^{Ch}Na+^{IV}(Mg^{2+},Fe^{2+}) = {}^{Ch}\square+{}^{IV}Al^{3+}$ exchange vector (Fig. 5b), again suggesting that cordierite does not contain Be and Li. As with sample 09-29, micro-Raman spectra do not show the 1383 cm^{-1} peak (Fig. S2) which is diagnostic for the presence of CO_2 (e.g. Kolesov & Geiger, 2000; Kaindl *et al*., 2006).

Alkali feldspar – It is generally perthitic and shows a X_{Ab} in the range 0.10-0.14.

Garnet – Garnet relicts shows X_{Ca} = 0.03, X_{Mg}=0.07-0.08 and X_{Mn}=0.14-0.15.

Sample 05-17

Microstructure

Sample 05-17 is a fine-grained biotite-cordierite gneiss consisting of cordierite (24 vol%), plagioclase (26 vol%), biotite (23 vol%) and quartz (18 vol%), with minor amounts of K-feldspar (4 vol%) and sillimanite (5 vol%). The main foliation is defined by discontinuous mesocratic layers consisting of biotite + sillimanite + cordierite alternated with leucocratic plagioclase + quartz ± alkali feldspar ± cordierite domains (Figs 3, 4h & S3g).

In the mesocratic domains, cordierite occurs as large poikiloblasts with abundant inclusions of sillimanite (Sil_1), biotite (Bt_1) and rounded quartz and plagioclase (Pl_1); Sil_1, Bt_1 and quartz never occur in mutual contact, but are always separated by cordierite (Figs 4i & S3g,h,i). In the leucocratic domains, cordierite is subhedral, with crystal faces locally well developed, and hosts only few inclusions (Fig. 4j). Both types of cordierite are partially replaced at their rim by fine-grained aggregates of white mica ± chlorite.

Alkali feldspar is rare and it is not uniformly distributed in the sample (Fig. 3); it is fine-grained and often shows cuspate shapes at the contact with adjacent grains of quartz, plagioclase or biotite (Fig. 4k). Scattered, cuspate shaped domains of quartz and plagioclase are also abundant in contact with rounded quartz, plagioclase and especially biotite (Figs 4k,j & S3h). Wherever not completely included in cordierite, Bt_1 flakes are clearly corroded by cordierite. Bt_1 is locally replaced by chlorite.

Mineral chemistry

Biotite – Bt_1 is quite homogeneous in composition, with Ti in the range 0.19-0.24 a.p.f.u. X_{Mg} and Al^{VI} slightly increase, in the range 0.37-0.40 and 0.27-0.37, respectively, with a concurrent Ti decrease. The small Bt_1 flakes included in cordierite poikiloblasts show, on average, a Ti content lower (0.19-0.22 a.p.f.u.) than the larger Bt_1 flakes defining the main foliation (0.20-0.24 a.p.f.u.) (Fig. 5a).

Plagioclase – The granoblastic Pl_1 is homogeneous, with X_{An} of 0.20-0.24 (Fig. 5c). No significant compositional variations have been observed for the rounded Pl_1 inclusions within cordierite poikiloblasts.

Cordierite – The X_{Mg} of poikiloblastic cordierite is homogeneous in the range 0.55-0.56, with the highest X_{Mg} generally observed in the core crowded of Sil_1, Bt_1, Pl_1 and quartz inclusions. The subhedral cordierite generally shows a slightly lower X_{Mg} than the poikiloblastic variety, in the range 0.54-0.55. Both cordierite varieties contain little Na (Na= 0.06-0.11 a.p.f.u.), with the highest contents in the subhedral type. Both cordierite types lie below the $^{Ch}Na+^{IV}Be^{2+} = {}^{Ch}\square+{}^{IV}Al^{3+}$ exchange vector, showing a (Si+Al) < 9.00 a.p.f.u. and (Mg+Fe) < 2.00 a.p.f.u. (Fig. 5b). This should be the evidence that cordierite contains some amounts of both Be and Li, as also suggested by the presence of Na, which has a strong correlation with these elements. There is no Raman 1383 cm^{-1} peak (Fig. S2) which is diagnostic of CO_2 (e.g. Kolesov & Geiger, 2000; Kaindl *et al*., 2006).

Alkali feldspar – The minor and fine-grained alkali feldspar in sample 05-17 has a X_{Ab} in the range 0.18-0.22.

P-T PSEUDOSECTION MODELLING

Strategies adopted to overcome uncertainties in the modelling of anatectic systems

In general, the *P-T* pseudosection modelling of melt-bearing systems is complicated by:

(i) the possibility that the system had experienced one or more episodes of melt loss and the actually measured bulk rock composition is somewhat different from that of the protolith. In this case, the prograde vs. retrograde *P-T* evolution of the anatectic rock should be constrained using different bulk compositions, each one representative of the equilibrium composition prior and after the episode of melt loss, respectively;

(ii) the difficulty to precisely estimate the H_2O content in the bulk, which is crucial in controlling the position of the *solidus* and the amount of melt that can be produced from a given source rock as a function of *P-T*.

These two problems are often overlooked and/or over-simplified in the modelling of anatectic systems, for example using a H_2O content simply derived from LOI (e.g. Sajeev *et al*., 2006; Imayama *et al*., 2012), or using a single bulk composition to derive the whole *P-T* evolution of the sample (e.g. Kali *et al*., 2010), or simply adding an arbitrary H_2O amount to the measured bulk rock composition in order to simulate the protolith composition (e.g. Streule *et al*., 2010). In order to minimize the uncertainties discussed previously, a different strategy for the *P-T* pseudosection modelling is described in the following.

Bulk compositions

The rationale followed in the modelling is that the actually observed mineral assemblages and modes are those corresponding to the final crystallization of the melt, i.e. at the *P-T* conditions where the *P-T* trajectory intersects the *solidus* of the system. As a consequence, the actual measured bulk composition (and H_2O content) can be used to model the *P-T* conditions of melt crystallization. Furthermore, because it is unlikely that melt loss could have occurred during crystallization (i.e. at decreasing temperature), the measured bulk composition can also be used to model the retrograde portion of the metamorphic evolution, from peak-*T* to the final melt crystallization (e.g. Clarke *et al*., 2007 and Indares *et al*., 2008 for further details). The bulk rock compositions (09-29a, 07-26a and 05-17a, Table 1) have been calculated by combining the mineral proportions obtained from the modal estimate of micro-XRF maps (Fig. 3) with mineral chemistry acquired at SEM-EDS. This

method was preferred to the conventional methods such as ICP-MS or XRF because the precise estimate of the modal percentage of hydrous minerals is required to derive the H_2O content in the bulk. The issue of the possible melt loss has been addressed by re-integrating to the actually measured bulk compositions an amount of melt sufficient to model a water saturated *solidus* in the *P* range of interest. These melt-reintegrated compositions (09-29b, 07-26b and 05-17b, Table 1) likely approximate those of protoliths containing the maximum possible amount of micas (see Indares *et al*., 2008 for further details), and can be therefore used to constrain the prograde portion of the metamorphic evolution, preceding the peak-*T* conditions.

H_2O amount

The H_2O content in the actually measured bulk has been estimated by combining mineral modes and compositions, considering that two hydrous phases are present in all the samples: biotite and cordierite. The amount of H_2O in biotite has been estimated using the Ti-H substitution scheme of White *et al*. (2007). Estimating the cordierite volatile content is challenging because of the facility of H_2O and/or CO_2 to be incorporated and/or released in its framework channels (e.g. Della Ventura *et al*., 2009). For modelling, it has been assumed that H_2O is the only volatile incorporated in the channels, which is confirmed by micro-Raman spectroscopy, as previously discussed. In addition, following the suggestion of Harley *et al*. (2002) that "cordierite formed through divariant melting in the low-*T* assemblage Crd + Bt + Sil + Qtz + Kfs + L is predicted to contain > 0.8 wt% H_2O at all pressures, and as high as 1.6 wt% H_2O at < 7 kbar", the H_2O content in cordierite (in terms of n = number of molecules of H_2O per formula unit of 18-oxygen volatile-free cordierite) has been fixed to a value (i.e. n = 0.55) such that $H_2O \leq 1.6$ wt%.

P-T pseudosection calculation

Two different pseudosections have been calculated for each sample, representing two end-member cases: (a) a first set of pseudosections was calculated using the actual measured bulk compositions (09-29a, 07-26a and 05-17a, Table 1) and it was used to constrain the *P-T* evolution from peak temperatures to the complete crystallization of the melt; (b) a second set of pseudosections was calculated using the melt-reintegrated compositions (09-29b, 07-26b and 05-17b, Table 1), and it was used to constrain the prograde *P-T* evolution (see Indares *et al*., 2008 and Groppo *et al*., 2012 for further details). Melt-reintegrated compositions likely approximating the protolith compositions of samples 09-29b, 07-26b and 05-17b have been calculated by reintegrating 38, 40 and 6 mol% of melt to the measured bulk compositions, respectively. These amounts of melt are those required to model a water saturated *solidus* in the *P* range of interest. The composition of reintegrated melt has been calculated at peak *P-T* conditions from pseudosections (a) (i.e. 810°C, 5 kbar for sample 09-29; 750°C, 4 kbar for samples 07-26 and 05-17). Details on the pseudosection calculation (model system, thermodynamic database, solution models) are given in the Appendix S1.

RESULTS

Interpretation of microstructures

All the samples show exceptionally well preserved microstructural evidence of melt-producing and melt-consuming reactions (e.g. Sawyer, 2008 and references therein):

i) *Melt pseudomorphs* - In all the samples, thin films of quartz, K-feldspar or plagioclase with cuspate shape are locally present between adjacent grains of quartz, biotite, cordierite or alkali feldspar (Figs 4f,k,j & S3a,h) and are interpreted as pseudomorphs of liquid-filled pores (e.g.

Holness & Clemens, 1999; Holness & Sawyer, 2008), thus suggesting that some melt crystallized in the interstices between grains.

ii) *Alkali feldspar* - Coarse-grained alkali feldspar poikiloblasts with abundant inclusions of Bt_1, rounded Pl_1 and quartz, and Sil_1 occur in samples 09-29 and 07-26 (Figs 4c,e & S3e). This microstructure suggests that alkali feldspar is a peritectic phase grown at the expenses of Pl_1, Bt_1, Sil_1 and quartz (e.g. Sawyer, 2008 and references therein). Modes and compositions of the leucocratic domains thus reflect the dominance of residual solid phases (e.g. peritectitc K-feldspar, unmolten quartz and plagioclase) after escape of some melt, rather than melt compositions. This implies that the leucocratic domains likely represent the evidence of once-active flow-networks through which melt has been lost from the system, rather than sites where melt was "stagnant" and crystallized *in situ* (e.g. Brown, 2002).

iii) *Cordierite* - In sample 09-29, poikiloblastic cordierite overgrows the mesocratic fine-grained Sil_1 + Bt_1 layers. Sil_1 and Bt_1 are never in mutual contact, but they are always separated by cordierite (Fig. 4b), thus suggesting that cordierite grew at the expenses of both Sil_1 and Bt_1. The peritectic nature of poikiloblastic cordierite is suggested by the local occurrence of melt pseudomorphs at the contact with the peritectic alkali feldspar (Fig. S3a). In the fold hinges cordierite porphyroblasts are undeformed (Fig. 4a), thus implying that the main foliation was developed prior to the partial melting event and that most of the biotite and sillimanite in sample 09-29 are remnants of the reactant assemblage (i.e. Bt_1 + Sil_1 + Pl_1 + Qtz) involved in the melt-producing reactions. The subhedral cordierite occurring in the leucocratic domains of sample 09-29 differs from the porphyroblastic peritectic cordierite being almost free of inclusions (Fig. 4a) and having a lower X_{Mg} content. This subhedral cordierite may be interpreted as a cotectic phase formed during melt crystallization.

Similarly to sample 09-29, in sample 05-17 the occurrence within poikiloblastic cordierite of abundant rounded inclusions of quartz, Sil_1, Pl_1 and corroded Bt_1, never in mutual contact (Figs 4i & S3g,i), suggests that cordierite grew at the expenses of all these phases, either as a peritectic phase (i.e. in the presence of melt) or at sub-*solidus* conditions or a combination of both. The subhedral cordierite occurring in the leucocratic domains grew certainly in the presence of melt, as testified by the occurrence of melt pseudomorphs of quartz separating cordierite from rounded plagioclase and/or biotite inclusions (Fig. 4j).

In sample 07-26, cordierite nodules are clearly grown at the expenses of fibrolitic sillimanite aggregates wrapped around by the main foliation (i.e. formed prior to the development of the main foliation) (Fig. 4d). This is consistent with a peritectic, mimetic, growth of cordierite during melt-producing reactions consuming sillimanite. The lozenge-shape of the original sillimanite aggregates and the fact that they are enveloped by the main foliation, however, strongly suggest that sillimanite aggregates are pseudomorphs after a former Al-rich phase, most likely andalusite (see Pitra & De Waal, 2001).

iv) *Garnet* - In sample 09-29, garnet relicts show very small dark and isotropic rounded inclusions, which are interpreted as preserved melt inclusions: this suggests that garnet is a peritectic phase. Although more detailed investigation is required to confirm the nature of these micrometric inclusions (e.g. Cesare *et al*., 2009; Ferrero *et al*., 2012), this hypothesis is confirmed by the local equilibrium relationships between garnet and peritectic alkali feldspar, only possible if the two minerals were in equilibrium during some stages of the sample metamorphic evolution. In sample 07-26, garnet occurs as very small (< 100 μm) relict crystals always set in large Pl_2

patches (Fig. S3f). In the absence of clear evidence that garnet grew during partial melting, doubts remain that it may be a sub-*solidus* relic.

v) *Microstructures related to back-reactions between solids and melt* - In sample 09-29, the rare plagioclase (Pl_2) + sillimanite (Sil_2) domains replacing alkali feldspar at its rim (Fig. S3b), the biotite (Bt_2) + quartz symplectitic microstructures developed at the interface between Bt_1 and alkali feldspar (Fig. S3c) and the discontinuous plagioclase (Pl_2) coronae around garnet relicts are interpreted as related to back-reactions between solid phases and melt during final melt crystallization. Similarly, in sample 07-26, the Pl_2 patches corroding both alkali feldspar poikiloblasts and Bt_1 flakes and in equilibrium with small idioblastic Bt_2 and Sil_2 (Figs 4g & S3f) may be interpreted as related to the final crystallization of the melt.

Basing on the interpretation of microstructures, the peak-*T* assemblages are inferred as: L + Kfs + Crd ± Grt (products) + Qtz + Bt + Pl + Als (reactants), with garnet being a peritectic phase only in sample 09-29.

P-T evolution

Peak-to retrograde P-T evolution

The retrograde *P-T* evolution has been inferred from *P-T* pseudosections calculated using the measured bulk-rock compositions (Figs 6a, 7a & 8a), which are dominated by five-variant fields, with minor four- and six-variant fields. The *solidus* of the system is always wet at < 3 kbar, whereas it is H_2O-undersaturated at > 3 kbar, but it is located at different *T* depending on the sample; the Crd-in boundary is uniformly located at < 6 kbar (at < 800°C). In all the calculated pseudosections, the coexistence of L + Qtz + Bt + Crd + Pl + Kfs + Als ± Grt ± Ilm is documented by narrow four- to six-variant fields between 680 and 850°C, with a slope of about 20 bar $°C^{-1}$, roughly corresponding to the univariant equilibrium Bt + Pl + Sil + Qtz = Crd/Grt + Ksf + L in the NKFMASH system (e.g. Clemens & Vielzeuf, 1987; Thompson, 2001), or Bt + Sil + Qtz = Crd + Kfs + L in the KFMASH system (Grant, 2004).

For all samples, the *P-T* conditions of melt crystallization have been constrained at 670-700°C, 2.5-3.0 kbar by the intersection between the *solidus* and the modelled mineral isomodes corresponding to the measured vol% of each phase (e.g. Indares *et al*., 2008; Groppo *et al*., 2010; Guilmette *et al*., 2011). The good convergence (on the *solidus*) of the modelled mineral isomodes for all samples argues in favour of the reliability of the model. At these *P-T* conditions the *solidus* is wet for sample 05-17 (H_2O < 0.5 vol%), whereas it is dry for the other two samples.

Peak-*T* conditions have been constrained based on the stability field of the observed peak assemblages and using the modelled compositional isopleths of biotite (Ti a.p.f.u. on the basis of 22 oxygens), cordierite (X_{Mg}) ± garnet (X_{Ca}). Due to the possible occurrence of diffusional homogenization at high temperatures, the highest X_{Mg} of cordierite, the highest Ti content of biotite and the lower X_{Ca} content of garnet provide minimum *T* constraints to the *P-T* conditions of the thermal peak (see Indares *et al*., 2008, Guilmette *et al*., 2011 and Groppo *et al*., 2010 for further details). The complete set of compositional isopleths and isomodes are shown in Figs S4, S6 & S8. The following peak *P-T* conditions have been obtained:

i) 800-820°C, 5.0-5.5 kbar for sample 09-29, as constrained by the peak assemblage L + Kfs + Crd (X_{Mg}=0.52-0.54) + Grt (X_{Ca}=0.028-0.029) + Qtz + Bt (Ti=0.28-0.31 a.p.f.u.) + Pl + Als;

ii) 760-780°C, 4.0-4.5 kbar for sample 07-26, as constrained by the peak assemblage L + Kfs + Crd (X_{Mg}=0.48-0.50) + Qtz + Bt (Ti=0.27-0.29 a.p.f.u.) + Pl + Als;

iii) 750-780°C, 4.2-5.0 kbar for sample 05-17, as constrained by the peak assemblage L + Kfs + Crd (X_{Mg}=0.54-0.56) + Qtz + Bt (Ti=0.23-0.24 a.p.f.u.) + Pl + Als.

At the estimated peak *P-T* conditions, the amount of melt predicted by the pseudosection modelling is very low, in the range 2-4 vol% (sample 09-29), 2-5 vol% (sample 07-26) and 1-3 vol% (sample 05-17). This is not consistent with the widespread evidence of melt-producing microstructures previously discussed for all samples and suggests that some melt was most probably extracted from the source rocks.

Prograde P-T evolution

In natural systems it is not possible to know exactly the total amount and composition of missing melt and the number of episodes of melt loss, therefore the exact missing melt cannot be added back to reconstruct the real sub-*solidus* protolith composition. As a consequence, the prograde portion of the *P-T* evolution of anatectic rocks is generally less well constrained than the retrograde one. However, the approach of melt reintegration used in this paper is useful to investigate the extended supra-*solidus* domain-topologies prior to melt loss, because it has been demonstrated that different scenarios of melt loss do not change significantly the supra-*solidus* topologies (White & Powell, 2002; Powell *et al*., 2005). Following this rationale, the prograde *P-T* evolution has been inferred from the *P-T* pseudosections calculated using the melt-reintegrated bulk-rock compositions (Figs 6b, 7b & 8b). The resulting supra-*solidus* topologies are very similar to those of the *P-T* pseudosections calculated using the measured bulk compositions, whereas they are significantly different in the sub-*solidus* domain and around the wet *solidus*, located at about 650-680°C. The melt-reintegrated *P-T* pseudosections predict different sub-*solidus* assemblages for the three samples: white mica is predicted to be abundant in the 09-29 and 07-26 prograde assemblages (i.e. two-mica metapelite/metagreywacke: 25-28 vol%), whereas the prograde assemblage of sample 05-17 does not contain white mica (i.e. biotite metapelite).

For the two-mica prograde assemblages (samples 09-29 and 07-26), the topologies around the *solidus* are mainly controlled by the intersection between the wet *solidus* and the white mica breakdown reactions (i.e. sub-*solidus* dehydration reaction and de-hydration melting reaction), located at about 650°C, 4 kbar and roughly corresponding to the invariant point IP1'' in the NKFMASH system (Spear *et al*., 1999). Two possibilities may thus be distinguished: (i) at $P > 4$ kbar, de-hydration melting of white mica occurs, resulting in the peritectic growth of K-feldspar, and (ii) at $P < 4$ kbar, the white mica breakdown occurs at sub-*solidus* conditions, thus implying that K-feldspar growth occurs in the absence of melt (e.g. Spicer *et al*., 2004; Buick *et al*., 2004).

For all samples, the prograde portion of the *P-T* trajectory should be consistent with microstructural observations suggesting that quartz, plagioclase (Pl_1), biotite (Bt_1) and sillimanite (Sil_1) are the reactants in the melt-producing reactions, whereas K-feldspar and cordierite ± garnet are the products. This implies that the prograde *P-T* paths should intersect the mineral isomodes accordingly (the complete set of compositional isopleths and isomodes for all the samples are reported in Figs S5, S7 & S9). All the relevant mineral isomodes have a positive slope in *P-T* space: as a consequence, any kind of heating path (i.e. either isobaric heating or decompressional heating) is in principle consistent with microstructural observations. However, there are some lines of evidence suggesting that a heating-dominated path is more likely than an heating and decompression path for all the samples:

(i) *Samples 09-29 and 07-26*: the slope of the modelled mineral isomodes is different from field to field. In particular, garnet isomodes have a subvertical negative slope in the L + Qtz + Bt

+ Pl + Kfs + Als + Grt field (Figs S5a & S7a), located between the white mica de-hydration melting reaction and the L + Qtz + Bt + Crd + Pl + Kfs + Als ± Grt field representing the peak assemblage. A prograde *P-T* trajectory intersecting such subvertical isomodes along a decompression path should not account for the development of garnet as a peritectitic phase as observed in both samples. On the contrary, a nearly isobaric path is more coherent with the observed microstructures. In addition, K-feldspar isomodes (Figs S5a & S7a) predict that at < 4 kbar, K-feldspar is produced through sub-*solidus* white mica breakdown, but it is consumed during melting at higher temperatures. This prediction gives an additional constraint to the prograde *P-T* trajectories, that should be located at > 4 kbar in order to be consistent with the microstructural observation that K-feldspar is a peritectic phase.

(ii) *Sample 05-17*: the lack of garnet in both the prograde and peak assemblage of this sample strictly constrains the prograde portion of its *P-T* path at < 5 kbar, thus implying a nearly isobaric heating path.

DISCUSSION

Peritectic vs. cotectic cordierite

Two different types of cordierite have been recognized on microstructural basis: (i) the most abundant type, occurring in the mesocratic domains, is poikiloblastic and it is crowded with small and rounded inclusions of quartz, Sil_1, Pl_1 and corroded Bt_1, never in mutual contact. It has been interpreted as a peritectic phase formed through reactions such as: $Bt_1 + Pl_1 + Sil_1 + Qtz = Crd/Grt + Kfs + L$; (ii) the second type occurs in the leucocratic domains and forms subhedral grains almost free of inclusions: it has been interpreted as a "cotectic" cordierite, likely grown during melt crystallization. Although compositionally very similar, the "cotectic" cordierite systematically shows a X_{Mg} lower than the peritectic variety.

In the pseudosection modelling, cordierite growth vs. cordierite consumption may be predicted according to how the calculated *P-T* paths intersect the cordierite isomodes (Fig. 9). For all samples, most cordierite growth occurred along the prograde *P-T* path (i.e. peritectic cordierite): at peak *P-T* conditions, the modelled amount of cordierite ranges between 10 vol% (sample 09-29), 17 vol% (sample 07-26) and 30 vol% (sample 05-17). However, the *P-T* pseudosections predict that cordierite growth also occurs along the first portion of the cooling and decompression paths. This "cotectic" process (i.e. occurring during melt crystallization) allows the formation of an additional 4-7 vol% of cordierite. Furthermore, the modelled X_{Mg} cordierite compositional isopleths also predict that "cotectic" cordierite has a X_{Mg} lower than the peritectic one. The thermodynamic modelling is thus perfectly in agreement with microstructural and minerochemical observations, and further confirms the interpretation of the peritectic vs. cotectic nature of cordierite.

Melt productivity during low-pressure anatexis

The influence of P and T

The results of the pseudosection modelling show that samples 09-29 and 07-26 have similar prograde assemblages (i.e. two-mica metapelite/metagreywacke) but experienced different peak *P-T* conditions (i.e. i.e. 800-820°C, 5-5.5 kbar vs. 750-800°C, 4-5 kbar); therefore, these samples are useful to discuss the influence of *P-T* on the melt productivity at constant mineralogical composition of the protolith. The melt isomodes modelled by the melt-reintegrated pseudosections (Figs 6b & 7b) show that, at peak *P-T* conditions, the amount of melt produced is approximately the

same for the two samples (~ 30-35 vol%), in spite of the difference of ~ 50°C between their peak-temperatures. A comparable production of melt is possible because the melt isomodes have a moderate dP/dT slope, meaning that the melt productivity increases as a function of both increasing *T* and decreasing *P*, in agreement with the predictions of theoretical models (e.g. Clemens & Vielzeuf, 1987) and the results of partial melting experiments (e.g. Vielzeuf & Holloway, 1988; Patiño-Douce & Harris, 1991). Overall, the modelled amount of melt produced by the two-mica samples is appreciably higher than the critical threshold of 7-10 vol% required for melt to be able to escape from its source (e.g. Rosenberg & Handy, 2005; Brown, 2007) thus suggesting that samples 09-29 and 07-26 may be interpreted as melt-depleted rocks (e.g. White & Powell, 2002; Sawyer, 2008).

The influence of the protolith composition

According to the pseudosection results, samples 07-26 and 05-17 experienced the same peak *P-T* conditions (i.e. 750-800°C, 4-5 kbar) but have different prograde assemblages (i.e. two-mica vs. biotite metapelites), therefore the two samples are useful to discuss which is the influence of bulk composition and mineral assemblage on the melt productivity at constant *P-T* conditions. The melt isomodes modelled by the melt-reintegrated pseudosections (Figs 7b & 8b) show that, at peak *P-T* conditions, the amount of melt produced is significantly different for the two samples (07-26: 30-35 vol% vs. 05-17: 8-10 vol%); in addition, the *solidus* for sample 05-17 is located at slightly higher temperatures (ca. 680°C at *P*= 5 kbar) than *solidus* of sample 07-26 (ca. 650°C). These data clearly demonstrate that the nature of the mica prograde assemblage is a very important parameter controlling the melt productivity at low pressure conditions.

Moreover, our results are perfectly in agreement with the results of experimental studies aimed to compare the melting behaviour of two-mica schists vs. biotite gneiss. All these studies predict that: (i) at pressure lower than 9 kbar, de-hydration melting of muscovite schists always takes place at lower temperature than that of biotite gneisses (Gardien *et al*., 1995; Patiño-Douce & Harris, 1998), and (ii) muscovite-bearing metapelites are 3-4 times more fertile at any given temperature than biotite gneisses over the same *T* interval (Gardien *et al*., 1995; Spicer *et al*., 2004). The most important geological consequence is that at relatively low pressure conditions, muscovite schists (e.g. samples 07-26 and 09-29) are able to generate significant amounts of leucogranitic melt at temperature of 650-700°C, whereas the interlayered biotite gneisses (e.g. sample 05-17) could remain unmolten or produce very limited amounts of melt (see also Buick *et al*., 1998).

The preservation of cordierite

The facility to incorporate/release volatiles within/outside the "channels" of its structure, makes it easily altered. It is thus very common, in anatectic rocks, to observe cordierite partially or completely retrogressed and replaced by fine-grained white mica ± chlorite or biotite aggregates of pinite. In contrast to this common occurrence, our samples contain spectacularly well preserved cordierite porphyroblasts, almost free of hydrous retrogression, except for a very thin white mica alteration rim locally observed in sample 05-17. To understand why this cordierite lacks retrograde re-hydration, it is necessary to discuss which are the processes responsible for the commonly observed cordierite alteration.

After its growth in the presence of melt, cordierite (either peritectic or cotectic) may be altered at different stages of its retrograde metamorphic evolution:

(i) at sub-*solidus* conditions, if a fluid phase is introduced from outside the system;

(ii) at the *solidus*, if it is wet, because in this case melt releases a free fluid phase during final crystallization, which may interact with the coexisting cordierite;

(iii) at supra-*solidus* conditions, due to retrograde H_2O exchange between cordierite and melt during cooling (i.e. through back-reactions). In the supra-*solidus* domain, the H_2O content of cordierite coexisting with a melt formed through biotite de-hydration melting is controlled by the distribution coefficient D_w as defined by Harley & Carrington (2001) [D_w = wt% $H_2O_{(melt)}$ / wt% $H_2O_{(Crd)}$]. Harley *et al*. (2002, their fig. 10) demonstrated that the isopleths of H_2O in the melt coexisting with a specific cordierite with a fixed H_2O content have a moderate d*P*/d*T* slope of about 15-16 bar °C^{-1}. Moving along these wt% $H_2O_{(melt)}$ isopleths in *P*-*T* space is equivalent to moving along a constant D_w curve, because both wt% $H_2O_{(melt)}$ and wt% $H_2O_{(Crd)}$ are fixed: this implies that, along these isopleths, cordierite and melt do not exchange H_2O to each other. As a consequence, Harley *et al*. (2002) concluded that migmatitic terranes evolving on post-peak cooling *P*-*T* paths with d*P*/d*T* slope of about 15-16 bar °C^{-1} are likely to avoid retrograde H_2O exchange between cordierite and melt. Any other type of retrograde *P*-*T* trajectory (i.e. d*P*/d*T* >> 15-16 bar °C^{-1} or d*P*/d*T* << 15-16 bar °C^{-1}) likely results in widespread back-reactions between cordierite and melt.

Following these assumptions, the lack of retrograde cordierite re-hydration in the studied samples should have been favoured by a combination of different factors:

(i) no significant hydration was experienced at sub-*solidus* conditions during the later stages of their metamorphic evolution;

(ii) the *solidus* of the system was almost dry, otherwise cordierite would be retrogressed at least at its rim. This assumption is confirmed by the results of the pseudosection modelling, showing that the *solidus* was dry for samples 09-29 and 07-26 (Figs 6a & 7a), whereas it was wet for sample 05-17, but with H_2O < 0.5 vol% (Fig. 8a), thus explaining the very limited retrogression at the cordierite rim in this sample;

(iii) there was no significant retrograde H_2O exchange between cordierite and melt during cooling at supra-*solidus* conditions, because of exhumation along a *P*-*T* path with a d*P*/d*T* of about 16-18 bar °C^{-1} (Fig. 9), thus maintaining the D_w equilibrium and preventing any back-reaction between cordierite and melt.

Crd-migmatites as source-rocks for the And-bearing leucogranites in central-east Himalaya

The cordierite-bearing anatectic gneisses and migmatites crop out at the upper structural levels of the HHC, immediately below the widespread Miocene leucogranites occurring as small plutons and/or networks of dykes south of the South Tibetan Detachment System (Fig. 1). The genesis of the Himalayan leucogranites is generally ascribed to decompression melting of the HHC in response to rapid exhumation within a extrusion-type or "channel flow"-type geodynamic context (e.g. Searle *et al*., 2010; Streule *et al*., 2010). However, peculiar andalusite- and cordierite-bearing two mica leucogranites reported from several localities in central-east Himalaya (e.g. Visonà & Lombardo, 2002 and reference therein) seem to contradict this genetic interpretation. Visonà *et al*. (2012) provide robust petrographic evidence that andalusite is an early magmatic (peritectic and/or cotectic) phase, thus suggesting that the andalusite leucogranites are produced by nearly isobaric low-*P* anatexis (< 4 kbar), rather than by decompression melting. According to their interpretation, likely source rocks for the andalusite leucogranites are the relatively cold muscovite-biotite rocks located above the hot, middle part, of the HHC (i.e. Barun Gneiss: Groppo *et al*., 2012).

The structural position of the cordierite-bearing migmatites as well as their *P*-*T* evolution which predicts a nearly isobaric prograde heating at low-*P*, are perfectly compatible with the hypothesis of Visonà *et al*. (2012). We therefore propose that the cordierite-bearing migmatites here investigated represent the source rocks for the genesis of the andalusite leucogranites. Further geochemical and/or isotopical studies could confirm or refute this hypothesis. As already emphasized by Visonà *et al*. (2012), however, the possible recognition of two opposite mechanisms (i.e. decompression melting vs. low-*P* isobaric heating) for the generation of the Himalayan leucogranites is of primary importance for the interpretation of the orogenic evolution of the whole Himalaya.

CONCLUSIONS

The results of this paper provide a key for the interpretation of the cordierite petrogenesis in migmatites from any low-pressure regional anatectic terrane:

(i) Peritectic vs. cotectic cordierite in low-*P* anatectic rocks may be distinguished on microstructural and compositional basis. The first type is poikiloblastic and includes those minerals which are the reactants in the cordierite-forming reaction (Qtz, Sil, Pl and Bt); the second type is subhedral, inclusion-free and shows a lower X_{Mg} than the coexisting peritectic variety.

(ii) The abundance and type of the micaceous minerals in the prograde assemblage is a basic parameter controlling the melt productivity at low-*P* conditions, being the two-mica protoliths significantly more fertile at any given temperature than biotite gneisses over the same temperature range.

(iii) The cordierite preservation is favoured by melt crystallization at a dry *solidus* and by exhumation along *P*-*T* paths with a peculiar d*P*/d*T* slope of about 15-18 bar $°C^{-1}$.

Furthermore, in the framework of Himalayan geology, the cordierite-bearing migmatites likely represent the source rocks for the Miocene andalusite-bearing leucogranites occurring at the upper structural levels of the Himalayan belt. Low-*P* isobaric heating rather than decompression melting is therefore the triggering process of the peculiar peraluminous magmatism.

ACKNOWLEDGEMENTS

Fieldwork was carried out thanks to financial support from PRIN Cofin 2004 and 2006. Laboratory work was supported by PRIN Cofin 2006 (2006040882-003). F.R. and C.G. acknowledge P. Pertusati, R. Carosi, C. Frassi, D. Iacopini, C. Montomoli and D. Visonà for discussion in the field while samples 05-17 and 07-26 were collected, and B. Lombardo for constructive discussions on Himalayan geology. Constructive comments by two anonymous reviewers considerably improved the paper; the helpful suggestions and editorial handling by Editor D. Robinson were greatly appreciated.

SUPPORTING INFORMATION

Appendix S1. Methods (μ-XRF fluorescence maps; Mineral chemistry; Pseudosection calculation)
Figure S1. Bulk compositions.
Figure S2. Micro-Raman spectra of cordierite.

Figure S3. Additional representative microstructures.
Figures S4-S9. Complete set of compositional isopleths and isomodes for the pseudosections of samples 09-29 (Figs S4 & S5), 07-26 (Figs S6 & S7) and 05-17 (Figs S8 & S9).
Table S1-S3. Representative SEM-EDS analyses of minerals.

REFERENCES

Barbey, P., Marignac, C., Montel, J.-M., Macaudière, J., Gasquet, D. & Jabbori, J., 1999. Cordierite growth textures and the conditions of genesis and emplacement of crustal granitic magmas: the Velay Granite Complex (Massif Central, France). *Journal of Petrology*, **10**, 1425–1441.

Bertoldi, C., Proyer, A., Garbe-Schönberg, D., Behrens, H. & Dachs, E., 2004. Comprehensive chemical analyses of natural cordierites: implications for exchange mechanisms. *Lithos*, **78**, 389–409.

Blümel, P. & Schreyer, W., 1977. Phase relations in pelitic and psammitic gneisses of the sillimanite-potash feldspar and cordierite-potash feldspar zones in the Moldanubicum of the Lam-Bodenmais area, Bavaria. *Journal of Petrology*, **18**, 431–459.

Bordet, P., 1961. *Recherches géologiques dans l'Himalaya du Népal, région du Makalu*. Editions du Centre National de la Recherche Scientifique, Paris, 275 p.

Borghi, A., Castelli, D., Lombardo, B. & Visonà, D., 2003. Thermal and baric evolution of garnet granulites from the Kharta region of S Tibet, E Himalaya. *European Journal of Mineralogy*, **15**, 401–418.

Brown, M., 2002. Retrograde processes in migmatites and granulites revisited. *Journal of Metamorphic Geology*, **20**, 24–40.

Brown, M., 2007. Crustal melting and melt extraction, ascent and emplacement in orogens: mechanism and consequences. *Journal of Geological Society of London*, **164**, 709–730.

Buick, I.S., Cartwright, I. & Harley, S.L., 1998. The retrograde *P*-*T*-t path for low-pressure granulites from the Reynolds Range, central Australia: petrological constraints and implications for low-*P*/high-*T* metamorphism. *Journal of Metamorphic Geology*, **16**, 511–529.

Buick, I.S., Stevens, G. & Gibson, R.L., 2004. The role of water retention in the anatexis of metapelites in the Bushveld Complex Aureole, South Africa: an experimental study. *Journal of Petrology*, **45**, 1777–1797.

Carrington, D.P. & Harley, S.L., 1995. Partial melting and phase relations in high-grade metapelites: an experimental petrogenetic grid in the KFMASH system. *Contributions to Mineralogy and Petrology*, **120**, 270–291.

Carrington, D.P. & Harley, S.L., 1996. Cordierite as a monitor of fluid and melt water contents in the lower crust : an experimental calibration. *Geology*, **24**, 647–650.

Cesare, B., Ferrero, S., Salvioli-Mariani, E., Pedron, D. & Cavallo, A., 2009. "Nanogranite" and glassy inclusions: the anatectic melt in migmatites and granulites. *Geology*, **37**, 627–630.

Clarke, D.B., 1995. Cordierite in felsic rocks: a synthesis. *Mineralogical Magazine*, **59**, 311–325.

Clarke, G.L., White, R.W., Lui, S., Fitzherbert, J.A. & Pearson, N.J., 2007. Contrasting behaviour of rare earth and major elements during partial melting in granulite facies migmatites, Wuluma Hills, Arunta Block, central Australia. *Journal of Metamorphic Geology*, **25**, 1–18.

Clemens, J.D. & Vielzeuf, D., 1987. Constraints on melting and magma production in the crust. *Earth and Planetary Science Letters*, **86**, 287–306.

Della Ventura, G., Bellatreccia, F., Cesare, B., Harley, S. & Piccinini, M., 2009. FTIR microspectroscopy and SIMS study of water-poor cordierite from El Hoyazo, Spain: Application to mineral and melt devolatilization. *Lithos*, **113**, 498–506.

Ferrero, S., Bartoli, O., Cesare, B., Salvioli Mariani, E., Cavallo, A., Groppo, C. & Battiston, S., 2012. Microstructures of melt inclusions in anatectic metasedimentary rocks. *Journal of Metamorphic Geology*, **30**, 303-322.

Fitzsimons, I.C.W., 1996. Metapelitic migmatites from Brattstrand Bluffs, east Antarctica – metamorphism, melting and exhumation of the mid-crust. *Journal of Petrology*, **37**, 395–414.

Gardien, V., Thompson, A.B., Grujic, D. & Ulmer, P., 1995. Experimental melting of biotite + plagioclase + quartz ± muscovite assemblages and implications for crustal melting. *Journal of Geophysical Research*, **100**, 15581–15591.

Goscombe, B. & Hand, M., 2000. Contrasting *P-T* paths in the Eastern Himalaya, Nepal: inverted isograds in a paired metamorphic mountain belt. *Journal of Petrology*, **41**, 1673–1719.

Goscombe, B., Gray, D. & Hand, M., 2006. Crustal architecture of the Himalayan metamorphic front in eastern Nepal. *Gondwana Research*, **10**, 232–255.

Grant, J.A., 2004. Liquid compositions from low-pressure experimental melting of pelitic rock from Morton Pass, Wyoming, USA. *Journal of Metamorphic Geology*, **22**, 65–78.

Groppo, C., Lombardo, B., Rolfo, F. & Pertusati, P., 2007. Clockwise exhumation path of granulitized eclogites from the Ama Drime range (Eastern Himalayas). *Journal of Metamorphic Geology,* **25,** 51-75.

Groppo, C., Rolfo, F. & Lombardo, B., 2009. *P-T* evolution across the Main Central Thrust Zone (Eastern Nepal): hidden discontinuities revealed by petrology. *Journal of Petrology*, **50**, 1149–1180.

Groppo, C., Rubatto, D., Rolfo, F. & Lombardo, B., 2010. Early Oligocene partial melting in the Main Central Thrust Zone (Arun Valley, eastern Nepal Himalaya). *Lithos*, **118**, 287–301.

Groppo, C., Rolfo, F. & Indares, A., 2012. Partial melting in the Higher Himalayan Crystallines of Eastern Nepal: the effect of decompression and implications for the "channel flow" model. *Journal of Petrology*, doi:10.1093/petrology/egs009.

Guilmette, C., Indares, A. & Hébert, R., 2011. High-pressure anatectic metapelites from the Namche Barwa, Eastern Himalayan Syntaxis: textural evidence for partial melting, phase equilibria modelling and tectonic implications. *Lithos*, **124**, 66–81.

Halpin, J.A., Clarke, G.L., White, R.W. & Kelsey, D.E., 2007. Contrasting P–T–t paths from the Neoproterozoic metamorphism in MacRobertson and kemp Lands, east Antarctica. *Journal of Metamorphic Geology*, **25**, 683–701.

Harley, S.L. & Carrington, D.P., 2001. The distribution of H_2O between cordierite and genetic melt: improved calibration of H_2O incorporation in cordierite and its application to high-grade metamorphism and crustal anatexis. *Journal of Petrology*, **42**, 1595–1620.

Harley, S.L., Thompson, P., Hensen, B.J. & Buick, I.S., 2002. Cordierite as a sensor of fluid conditions in high-grade metamorphism and crustal anatexis. *Journal of Metamorphic Geology*, **20**, 71–86.

Harley, S.L., 1994. Cordierite as a sensor of fluid and melt distribution in crustal metamorphism. *Mineralogical Magazine*, **58a**, 374–375.

Holland, T.J.B.& Powell, R., 2001. Calculation of phase relations involving haplogranitic melts using an internally consistent thermodynamic dataset. *Journal of Petrology*, **42**, 673–683.

Holness, M.B. & Clemens, J.D., 1999. Partial melting of the Appin Quartzite driven by fracture controlled H_2O infiltration in the aureole of the Ballachulish Igneous Complex, Scottish Highlands. *Contributions to Mineralogy and Petrology*, **136**, 154–168.

Holness, M.B. & Sawyer, E.W., 2008. On the pseudomorphing of melt-filled pores during the crystallization of migmatites. *Journal of Petrology*, **49**, 1343–1363.

Imayama, T., Takeshita, T. & Arita, K., 2010. Metamorphic *P-T* profile and *P-T* path discontinuity across the far-eastern Nepal Himalaya: investigation of channel flow models. *Journal of Metamorphic Geology*, **28**, 527–549.

Imayama, T., Takeshita, T., Yi, K., Cho, D.-Y., Kitajima, K., Tsutsumi, Y., Kayama, M., Nishido, H., Okumura, T., Yagi, K., Itaya, T. & Sano, Y., 2012. Two-stage partial melting and contrasting cooling history within the Higher Himalayan Crystalline Sequence in the far-eastern Nepal Himalaya. *Lithos*, **134-135**, 1–22.

Indares, A., White, R.W. & Powell, R., 2008. Phase equilibria modelling of kyanite-bearing anatectic paragneiss from the central Grenville Province. *Journal of Metamorphic Geology*, **26**, 815–836.

Johnson, T.E., Hudson, N.F.C. & Droop, G.T.R., 2001. Partial melting in the Inzie head gneisses: the role of water and a petrogenetic grid in KFMASH applicable to anatectic politic migmatites. *Journal of Metamorphic Geology*, **19**, 99–118.

Johnson, T., Brown, M., Gibson, R. & Wing, B., 2004. Spinel–cordierite symplectites replacing andalusite: evidence for melt-assisted diapirism in the Bushveld Complex, South Africa. *Journal of Metamorphic Geology*, **22**, 529–545.

Johnson, T.E., White, R.W. & Powell, R., 2008. Partial melting of metagreywacke: a calculated mineral equilibria study. *Journal of Metamorphic Geology*, **26**, 837–853.

Kaindl, R., Tropper, P., & Deibl, I., 2006. A semi-quantitative technique for determination of CO_2 in cordierite by Raman spectroscopy in thin sections. *European Journal of Mineralogy*, **18**, 331–335.

Kali, E., Leloup, P.H., Arnaud, N., Mahèo, G., Dunyi, L., Boutonnet, E., Van der Woerd, J., Liu, X., Liu-Zeng, J. & Li, H., 2010. Exhumation history of the deepest central Himalayan rocks, Ama Drime range: Key pressure‐temperature‐deformation‐time constraints on orogenic models. *Tectonics*, **29**, TC2014.

Kelsey, D.E., White, R.W., Powell, R., Wilson, C.J.L. & Quinn, C.D., 2003. New constraints on metamorphism in the Rauer Group, Prydz Bay, east Antarctica. *Journal of Metamorphic Geology*, **21**, 739–759.

Kolesov, B.A. & Geiger, C.A., 2000. Cordierite II: The role of CO_2 and H_2O. *American Mineralogist*, **85**, 1265–1274.

Le Fort, P., 1975. Himalaya: the collided range. Present knowledge of the continental arc. *American Journal of Science*, **275A,** 1–44.

Lombard, A., 1958. Un itinéraire géologique dans l'est du Nepal (massif du Mont Everest). Mémoire de la Societé Helvétique des Sciences Naturelles, **82**.

Lombardo, B., Pertusati, P. & Borghi, A., 1993. Geology and tectono-magmatic evolution of the eastern Himalaya along the Chomolungma-Makalu transect. In: Treloar, P.J. & Searle, M.P. (eds.) *Himalayan Tectonics*. Geological Society of London, Special Publication, **74**, London, 341–355.

Lombardo, B. & Rolfo, F., 2000. Two contrasting eclogite types in the Himalayas: implications for the Himalayan orogeny. *Journal of Geodynamics,* **30,** 37-60.

Lombardo, B., Rolfo, F. & Compagnoni, R., 2000. Glaucophane and barroisite eclogites from the Upper Kaghan Nappe: implications for the metamorphic history of the NW Himalaya. In: Khan, M.A., Treloar, P.J., Searle, M.P. & Jan, M.Q. (eds) *Tectonics of the Nanga Parbat Syntaxis and the Western Himalaya*, Geological Society of London, Special Publication, **170,** London, 411-430.

Montel, J.M. & Vielzeuf, D., 1997. Partial melting of metagreywackes, Part II. Compositions of minerals and melts. *Contribution to Mineralogy and Petrology*, **128**, 176–196.

Mosca, P., Groppo, C. & Rolfo, F. (2011). Geological and structural architecture of the Kangchenjunga region in Eastern Nepal. *Journal of Nepal Geological Society* (in press).

Patiño Douce, A.E. & Harris, N., 1998. Experimental constraints on Himalayan anatexis. *Journal of Petrology*, **39**, 689–710.

Peirera, M.D. & Bea, F., 1994. Cordierite-producing reactions in the Pena Negra complex, Avila batholith, Central Spain: the key role of cordierite in low-pressure anatexis. *Canadian Mineralogist*, **32**, 763–780.

Pitra, P. & De Waal, S.A., 2001. High-temperature, low-pressure metamorphism and development of prograde symplectites, Marble Hall Fragment, Bushveld Complex (South Africa). *Journal of Metamorphic Geology*, 19, 311-325.

Pognante, U. & Benna, P., 1993. Metamorphic zonation, migmatization, and leucogranites along the Everest transect (Eastern Nepal and Tibet): record of an exhumation history. In: Treloar, P.J. & Searle, M.P. (eds.) *Himalayan Tectonics*. Geological Society of London, Special Publication, **74**, London, 323–340.

Powell, R., Guiraud, M. & White, R.W., 2005. Truth and beauty in metamorphic phase equilibria: conjugate variables and phase diagrams. *Canadian Mineralogist*, **43**, 21–33.

Rosenberg, C.L. & Handy, M.R., 2005. Experimental deformation of partially melted granite revisited: implications for the continental crust. *Journal of Metamorphic Geology*, **23**, 19–28.

Sajeev, K., Santosh, M. & Kim, H.S., 2006. Partial melting and P–T evolution of the Kodaikanal Metapelite Belt, southern India. *Lithos*, **92**, 465-483.

Sawyer, E.W., 2008. *Atlas of migmatites*. The Canadian Mineralogist, Special Publication, **9**, NRC Research Press, Ottawa, Ontario, 371p.

Searle, M.P., Law, R.D., Godin, L., Larson, K.P., Streule, M.J., Cottle, J.M. & Jessup, M.J., 2008. Defining the Himalayan Main Central Thrust in Nepal. *Journal of the Geological Society of London*, **165**, 523–534.

Searle, M.P., Cottle, J.M., Streule, M.J. & Waters, D.J., 2010. Crustal melt granites and migmatites along the Himalaya: melt source, segregation, transport and granite emplacement mechanisms. *Earth and Environmental Science Transactions of the Royal Society of Edinburgh*, **100**, 219–233.

Spear, F.S., Kohn, M.J. & Cheney, J.T., 1999. *P-T* paths from anatectic pelites. *Contributions to Mineralogy and Petrology*, **134**, 17–32.

Spicer, E.M., Stevens, G. & Buick, I.S., 2004. The low-pressure partial-melting behaviour of natural boron-bearing metapelites from the Mt. Stafford area, central Australia. *Contribution to Mineralogy and Petrology*, **148**, 160–179.

Stevens, G., Clemens, J.D. & Droop, G.T.R., 1995. Hydrous Cordierite in granulites and crustal magma production. *Geology*, **23**, 925–928.

Stevens, G., Clemens, J.D. & Droop, G.D.R., 1997. Melt production during granulite-facies anatexis: experimental data from "primitive" metasedimentary protoliths. *Contributions to Mineralogy and Petrology*, **128**, 352–370.

Streule, M.J., Searle, M.P., Waters, D.J. & Horstwood, M.S.A., 2010. Metamorphism, melting and channel flow in the Greater Himalaya Sequence and Makalu leucogranite: constraints from thermobarometry, metamorphic modelling and U-Pb geochronology. *Tectonics*, **29**, TC5011.

Thompson, P., Harley, S.L. & Carrington, D.P., 2001. The distribution of H_2O-CO_2 between cordierite and granitic melt under fluid saturated conditions at 5 kbar and 900°C. *Contributions to Mineralogy and Petrology*, **142**, 107–118.

Thompson, A.B., 2001. Clockwise P–T paths for crustal melting and H_2O recycling in granite source regions and migmatite terrains. *Lithos*, **56**, 33–45.

Vielzeuf, D. & Holloway, J.R., 1988. Experimental determination of the fluid-absent melting relations in the pelitic system. *Contributions to Mineralogy and Petrology*, **98**, 257–276.

Vielzeuf, D. & Montel, J.M., 1994. Partial melting of metagreywacke. Part I: fluid absent experiments and phase relationships. *Contributions to Mineralogy and Petrology*, **117**, 375–393.

Visonà, D. & Lombardo, B., 2002. Two mica- and tormaline leucogranites from the Everest-Makalu region (Nepal-Tibet): Himalayan leucogranite genesis by isobaric heating? *Lithos*, **62**, 125–150.

Visonà, D., Carosi, R., Montomoli, C., Tiepolo, M. & Peruzzo, L., 2012. Miocene andalusite leucogranite in central-east Himalaya (Everest-Masang Kang area): low-pressure melting during heating. Lithos, in press, doi: 10.1016/j.lithos.2012.04.012.

Visser, D., Kloprogge, J.T. & Maijer, C., 1994. An infrared spectroscopic (IR) and light element (Li, Be, Na) study of cordierites from the Bamble Sector, South Norway. *Lithos*, **32**, 95–107.

Vry, J.K., Brown, P.E. & Valley, J.W., 1990. Cordierite volatile content and the role of CO_2 in high-grade metamorphism. *American Mineralogist*, **75**, 71–88.

Waters, D.J., 1988. Partial melting and the formation of granulite facies assemblages in Namaqualand, South Africa. *Journal of Metamorphic Geology*, **6**, 387–404.

Wei, C. & Powell, R., 2004. Calculated phase relations in high-pressure metapelites in the system NKFMASH (Na_2O-K_2O-FeO-MgO-Al_2O_3-SiO_2-H_2O). *Journal of Petrology*, **45**,183–202.

White, R.W. & Powell, R., 2002. Melt loss and the preservation of granulite facies mineral assemblages. *Journal of Metamorphic Geology*, **20**, 621–632.

White, R.W. & Powell, R., 2011. On the interpretation of retrograde reaction textures in granulite facies rocks. *Journal of Metamorphic Geology*, **29**, 131–149.

White, R.W., Powell, R. & Holland, T.J.B., 2001. Calculation of partial melting equilibria in the system Na_2O-CaO-K_2O-FeO-MgO-Al_2O_3-SiO_2-H_2O (NCKFMASH). *Journal of Metamorphic Geology*, **19**, 139–153.

White, R.W., Powell, R. & Clarke, G.L., 2003. Partial melting at low pressures: Migmatites from Mt Stafford, central Australia. *Journal of Petrology*, **44**, 1937–1960.

White, R.W., Powell, R. & Clarke, G.L., 2002. The interpretation of reaction textures in Fe-rich metapelitic granulites of the Musgrave Block, central Australia: constraints from mineral equilibria calculations in the system K_2O-FeO-MgO-Al_2O_3-SiO_2-H_2O-TiO_2-Fe_2O_3. *Journal of Metamorphic Geology*, **20**, 41–55.

White, R.W., Powell, R. & Holland, T.J.B., 2007. Progress relating to calculation of partial melting equilibria for metapelites. *Journal of Metamorphic Geology*, **25**, 511–527.

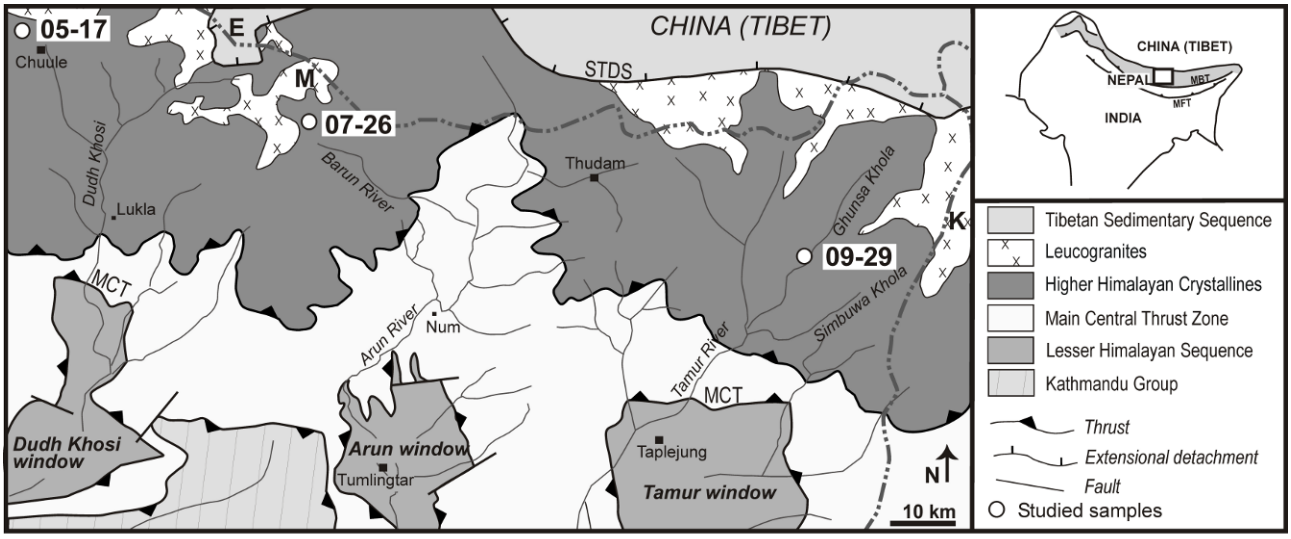

Fig. 1 – Simplified geological map of the central-eastern sector of the Himalayan belt (modified from Goscombe *et al*., 2006, Groppo *et al*., 2009 and Mosca *et al*., 2011) showing sample locations (white circles). The double dashed line is the approximate political boundary between Nepal to the south, west, China (Tibet) to the north, India (Sikkim) to the east. MCT: Main Central Thrust, STDS: South Tibetan Detachment System; E: Everest, K: Kangchenjunga, M: Makalu. Inset shows the location of the study area (black rectangle) in the framework of the Himalayan chain. The grey shaded belt approximates the location of the Higher Himalayan Crystallines. MFT: Main Frontal Thrust; MBT: Main Boundary Thrust.

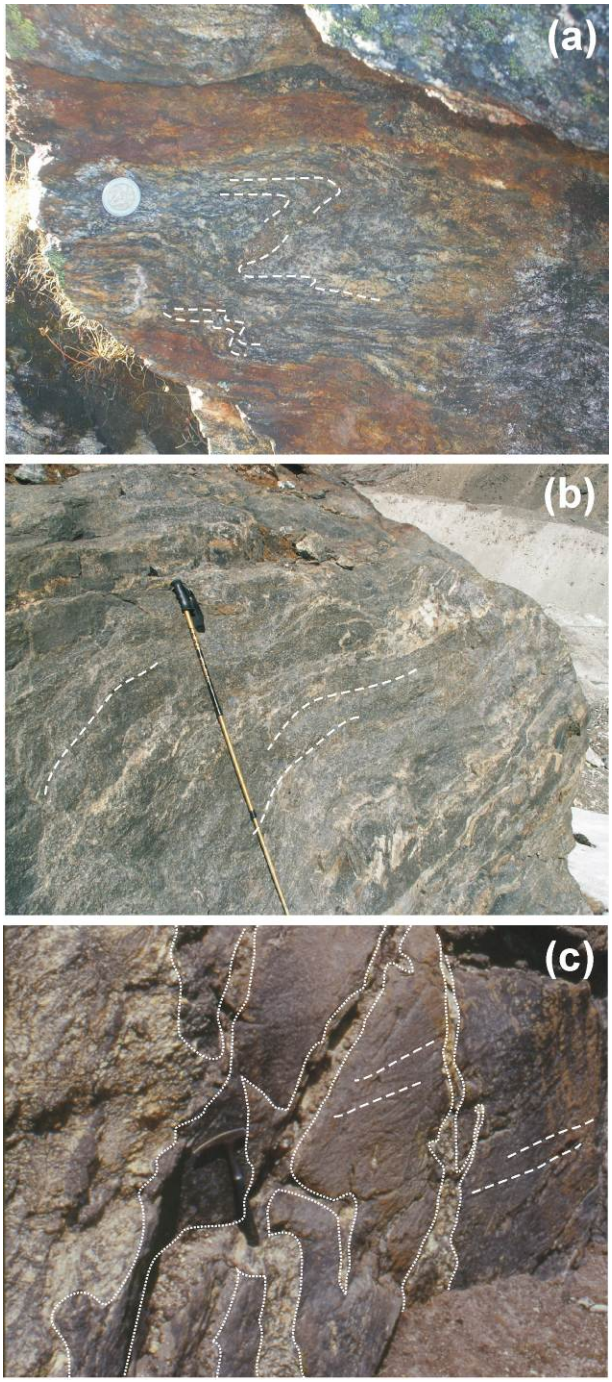

Fig. 2 – Field occurrence of samples. (a) Sample 09-29 (Ghunsa Khola, 3200 m a.s.l.): the main foliation, defined by millimetric leucocratic quartzo-feldspathic domains alternating with dark cordierite + biotite + sillimanite layers, is deformed by asymmetric folds, gently plunging to the NE, and showing sub-horizontal axial planes. (b) Sample 07-26 (Barun valley, 5130 m a.s.l.): fine-grained biotite gneiss with rare centimetric quartzo-feldspatic layers. (c) Sample 05-17 (Bhote Khosi, 5100 m a.s.l.): fine-grained biotite gneiss crosscut by metric to decimetric granitic dykes (note the hammer in the centre for scale).

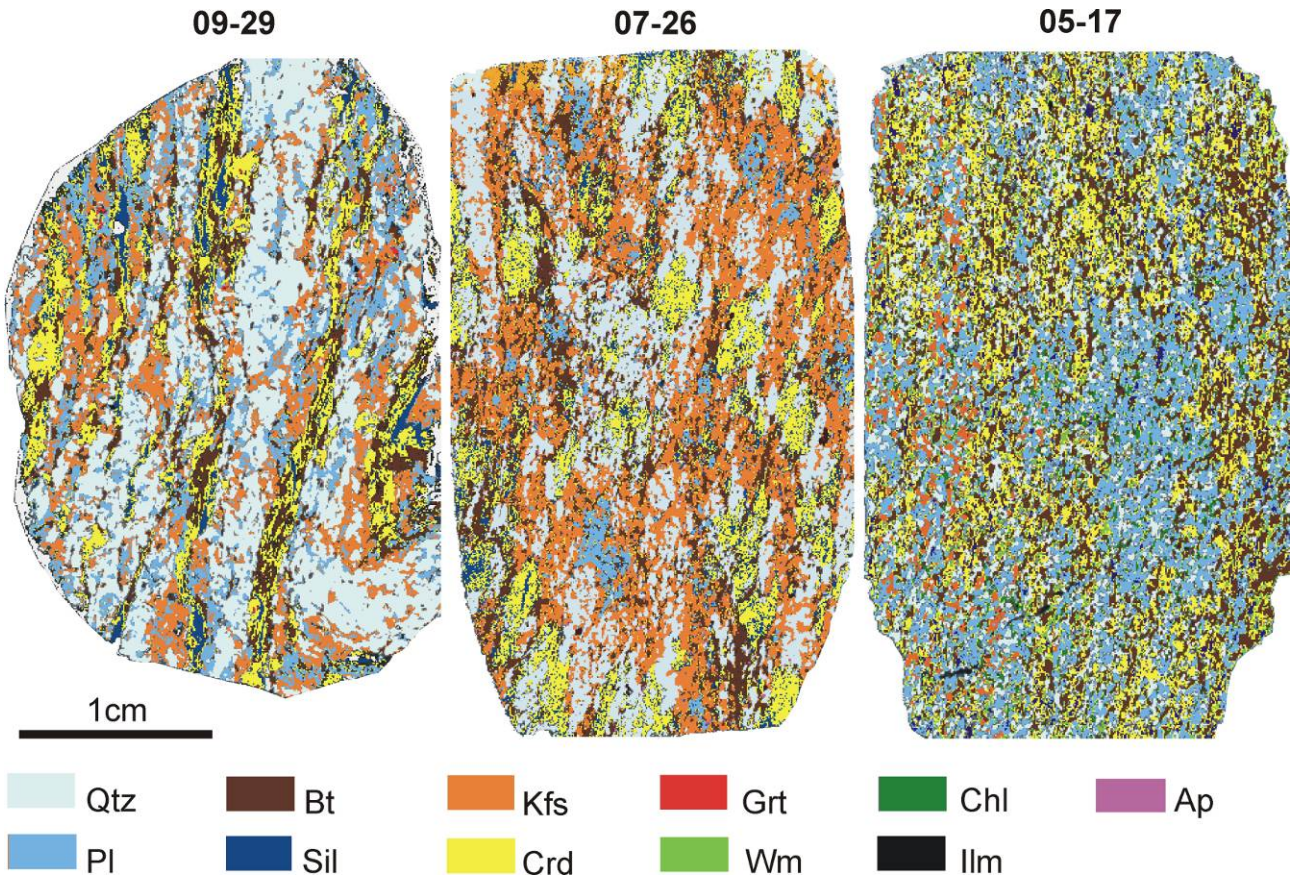

Fig. 3 – Major elements μ-XRF maps of the whole thin sections of samples 09-29, 07-26 and 05-17. Note the different proportion between plagioclase and alkali feldspar.

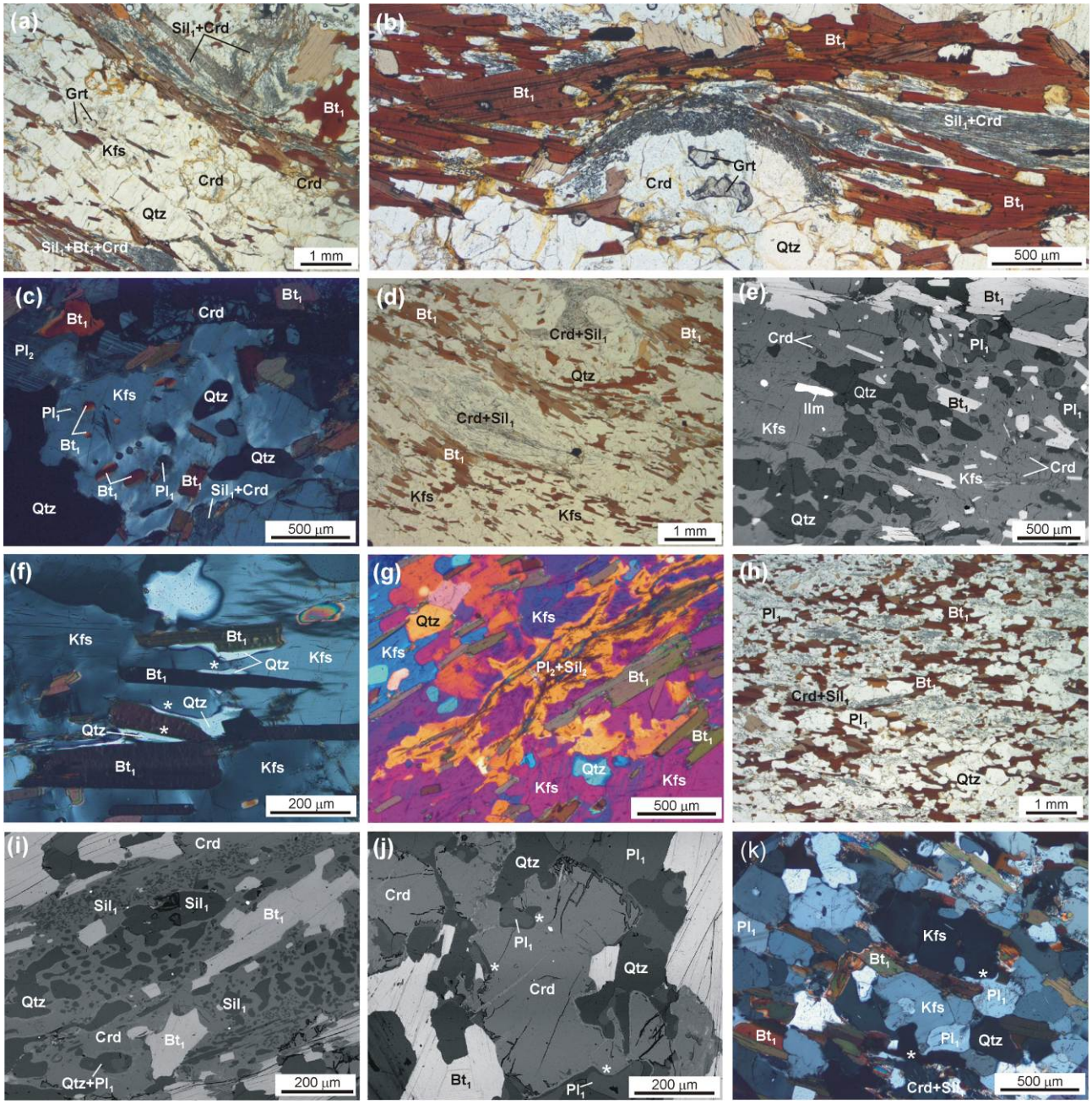

Fig. 4 – Representative microstructures of samples. **Sample 09-29**: (a) Leucocratic quartzo-feldspatic domains alternated to mesocratic biotite + sillimanite + cordierite layers. Cordierite occurs in two different positions: as large poikiloblasts in the mesocratic domains and as subhedral crystals in the leucocratic layers. Plane Polarized Light (PPL). (b) Detail of mesocratic layer showing poikiloblastic cordierite growing at the expenses of biotite and sillimanite, which are not in mutual contact. Cordierite also replaces garnet. PPL. (c) Detail of large alkali feldspar poikiloblast, showing rounded inclusions of biotite, plagioclase and quartz. Crossed Polarized Light (XPL). **Sample 07-26**. (d) Cordierite nodules are wrapped around by the discontinuous foliation defined by the alignment of biotite. Cordierite nodules have a lozenge shape and isolate sillimanite aggregates from the matrix. PPL. (e) Alkali feldspar poikiloblast with rounded inclusions of quartz, cordierite and biotite. Back Scattered Electron image (BSE). (f) Detail of pseudomorphs of liquid-filled pores consisting of optically continuous crystals of quartz with low dihedral angles (see asterisks) in contact with alkali feldspar and biotite. XPL. (g) Detail of plagioclase + sillimanite (Pl_2+Sil_2) patch partially replacing alkali feldspar. XPL with first-order red plate. **Sample 05-17**: (h) The discontinuous foliation is defined by the alignment of biotite flakes, isolated from sillimanite by cordierite poikiloblasts. PPL. (i)

Cordierite poikiloblast (mesocratic domain) with inclusions of rounded quartz, sillimanite, plagioclase and biotite. BSE image. (j) Subhedral cordierite (leucocratic domain). Asterisks indicate pseudomorphs of liquid-filled pores consisting of quartz with low dihedral angles against plagioclase and cordierite. BSE image. (k) Detail of leucocratic layer: alkali feldspar and plagioclase show cuspate shapes at the contact with adjacent grains of quartz and biotite. XPL.

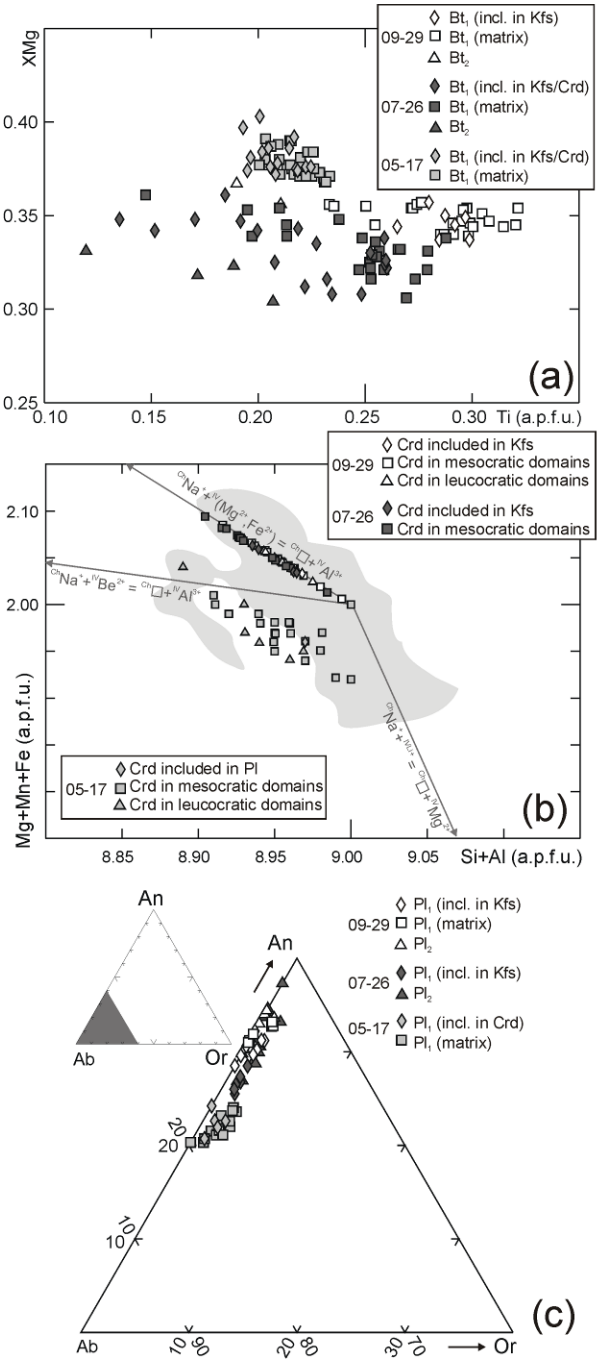

Fig. 5 – Compositional diagrams for biotite, cordierite and plagioclase. (a) Ti (a.p.f.u.) vs. X_{Mg} diagram for biotite. (b) Si+Al vs. Mg+Mn+Fe diagram (Bertoldi *et al*., 2004) for cordierite, with the indication of the main exchange vectors, useful to recognize the presence of Li and/or Be in the analyzed cordierite. (c) Ab-An-Or diagram showing the composition of different generations of plagioclase.

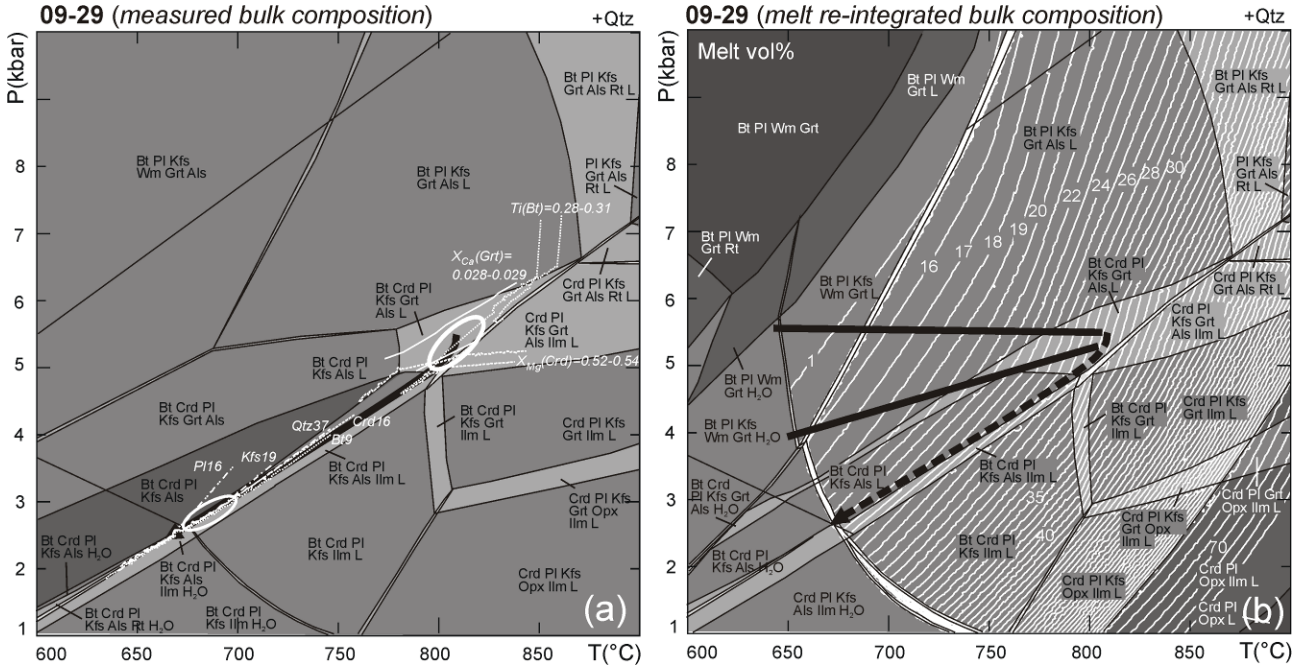

Fig. 6 – (a) *P-T* pseudosection for sample 09-29 in the MnNKCFMASTH system, calculated using the measured bulk composition 09-29a (Table 1). The variance of the fields varies from two (i.e. ten phases, white fields) to six (i.e. six phases, darker grey fields). White ellipses constrain the *P-T* conditions of final melt crystallization (white ellipse at lower *T*) and the peak P_{min}-T_{min} conditions (white ellipse at higher *T*) as inferred from mineral isomodes and compositional isopleths of biotite (Ti), cordierite (X_{Mg}) and garnet (X_{Ca}), reported as white lines. The black arrow is the resulting retrograde *P-T* path. The entire set of isopleths is available at Fig. S4. (b) *P-T* pseudosection for sample 09-29 calculated using the melt-reintegrated bulk composition 09-29b (Table 1) obtained from reintegration of 38 mol% of melt. The variance of the fields varies from two (i.e. ten phases, white fields) to seven (i.e. five phases, darker grey fields). The dashed arrow is the same as in (a). The two black lines constrain the prograde *P-T* path, as suggested by isomodes and compositional isopleths reported in Fig. S5. Melt isomodes are reported as white lines.

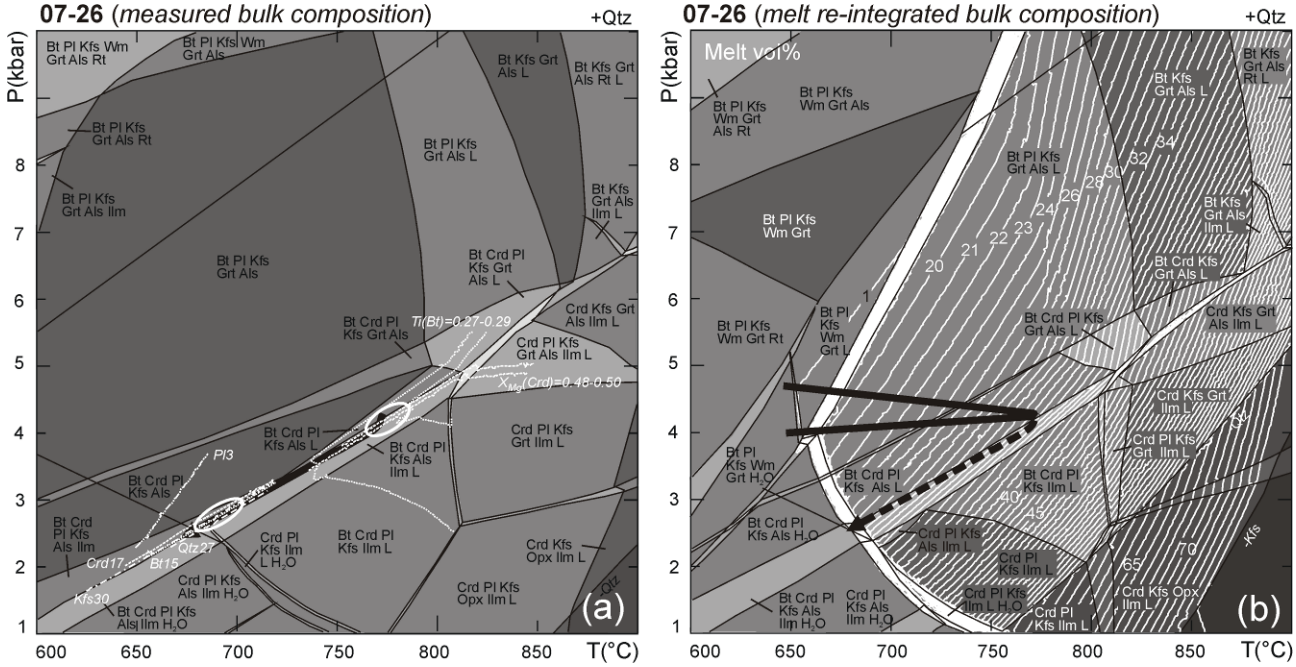

Fig. 7 – (a) *P-T* pseudosection for sample 07-26 in the MnNKCFMASTH system, calculated using the measured bulk composition 07-26a (Table 1). The variance of the fields varies from two (i.e. 10 phases, white fields) to six (i.e. six phases, darker grey fields). White ellipses constrain the *P-T* conditions of final melt crystallization (white ellipse at lower *T*) and the peak P_{min}-T_{min} conditions (white ellipse at higher *T*) as inferred from mineral isomodes and compositional isopleths of biotite (Ti) and cordierite (X_{Mg}), reported as white lines. The black arrow is the resulting retrograde *P-T* path. The entire set of isopleths is available at Fig. S6. (b) *P-T* pseudosection for sample 07-26 calculated using the melt-reintegrated bulk composition 07-26b (Table 1) obtained from re-integration of 40 mol% of melt. The variance of the fields varies from two (i.e. ten phases, white fields) to seven (i.e. five phases, darker grey fields). The dashed arrow is the same as in (a). The two black lines constrain the prograde *P-T* path, as suggested by isomodes and compositional isopleths reported in Fig. S7. Melt isomodes are reported as white lines.

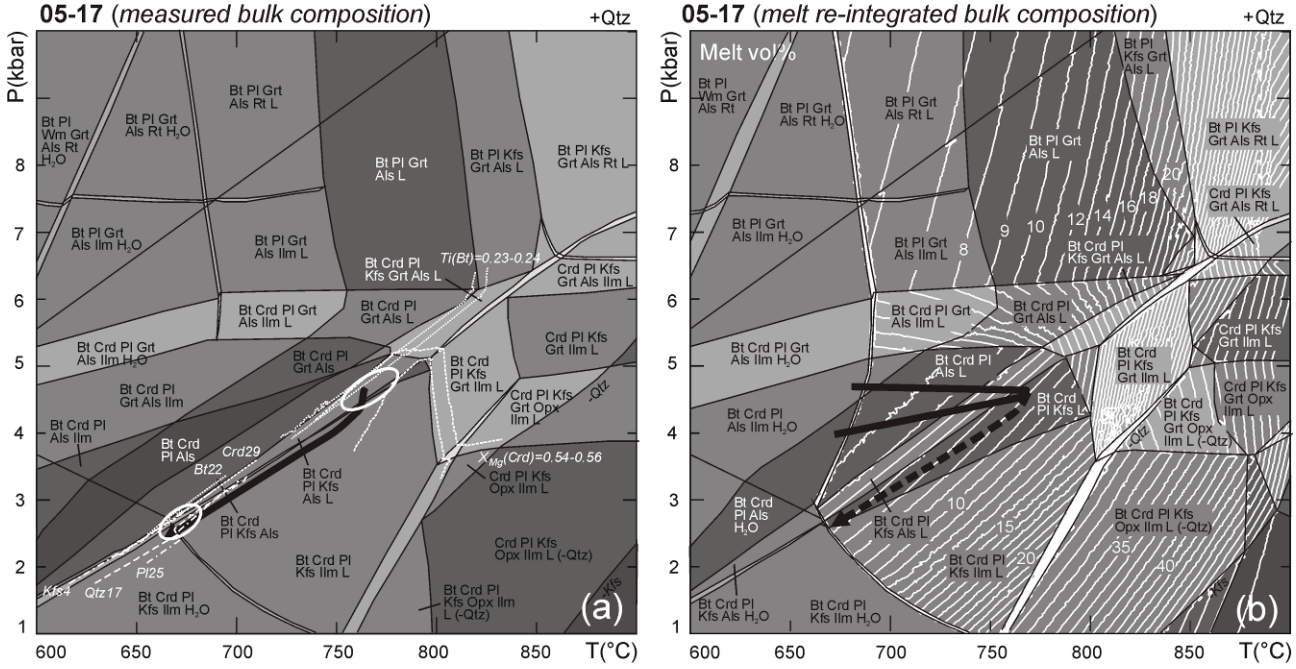

Fig. 8 – (a) *P-T* pseudosection for sample 05-17 in the MnNKCFMASTH system, calculated using the measured bulk composition 05-176a (Table 1). The variance of the fields varies from two (i.e. ten phases, white fields) to seven (i.e. five phases, darker grey fields). White ellipses constrain the *P-T* conditions of final melt crystallization (white ellipse at lower *T*) and the peak P_{min}-T_{min} conditions (white ellipse at higher *T*) as inferred from mineral isomodes and compositional isopleths of biotite (Ti) and cordierite (X_{Mg}), reported as white lines. The black arrow is the resulting retrograde *P-T* path. The entire set of isopleths is available at Fig. S8. (b) *P-T* pseudosection for sample 05-17 calculated using the melt-reintegrated bulk composition 05-17b (Table 1) obtained from re-integration of 6 mol% of melt. The variance of the fields varies from two (i.e. ten phases, white fields) to seven (i.e. five phases, darker grey fields). The dashed arrow is the same as in (a). The two black lines constrain the prograde *P-T* path, as suggested by isomodes and compositional isopleths reported in Fig. S9. Melt isomodes are reported as white lines.

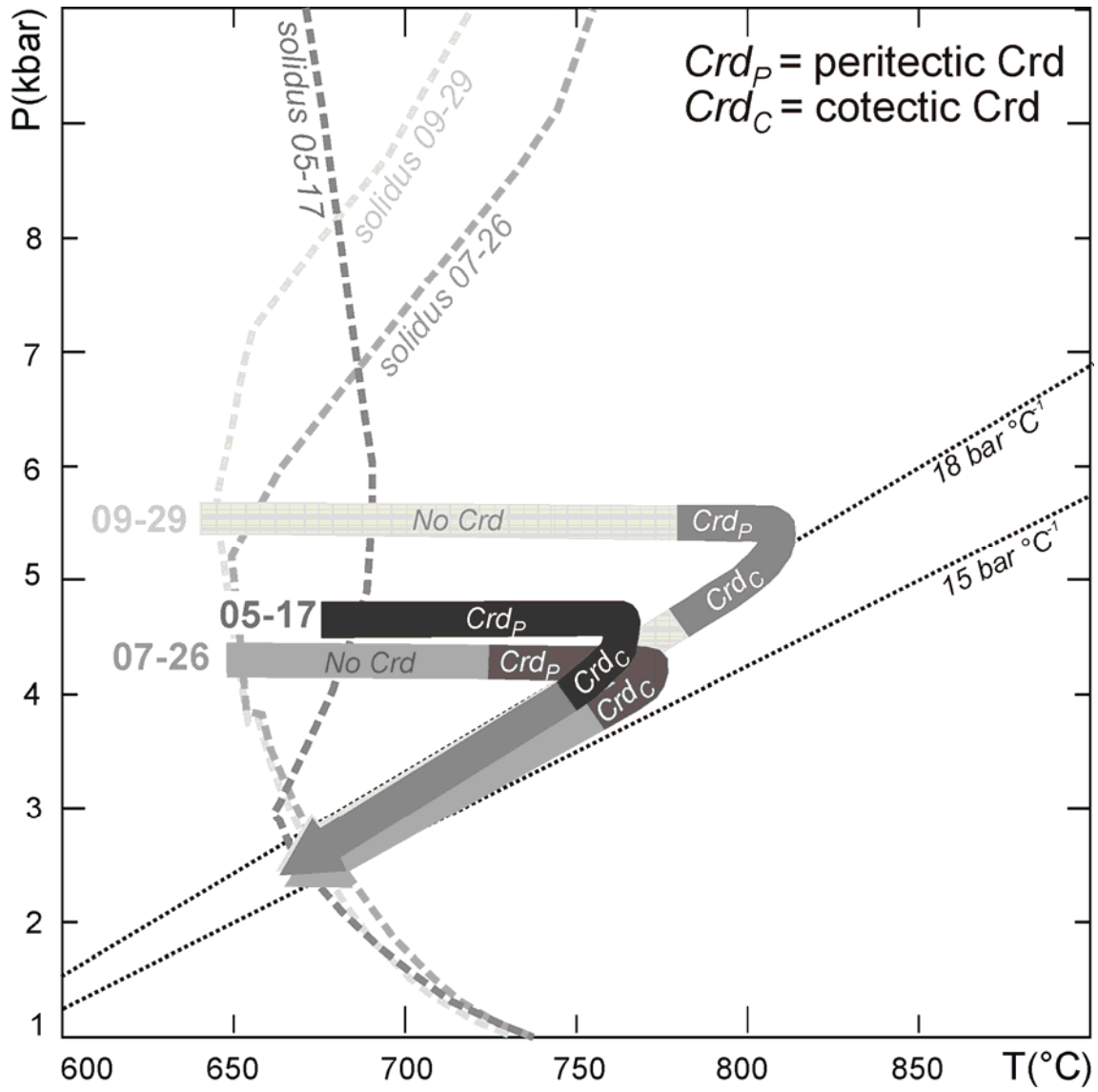

Fig. 9 - *P-T* diagram showing the *P-T* paths calculated for samples 09-29, 07-26 and 05-17 and the correspondent *solidus* curves derived from Figs 6b, 7b & 8b, respectively. The darker portions of each *P-T* path correspond to those *P-T* conditions at which cordierite growth is predicted by the *P-T* pseudosection modelling. Cordierite grows as a peritectic phase (Crd_P) at increasing temperature and as a cotectic phase (Crd_C) at decreasing temperature. The cooling and decompression portions of the calculated *P-T* paths occur along 15-18 bar $°C^{-1}$ gradients, thus favouring the cordierite preservation.

Table 1 - Bulk compositions measured (a) vs. melt re-integrated (b), and composition of the re-integrated melt (m) (the amount of added melt is in mol%) calculated at the indicated P-T conditions

	09-29			07-26			05-17		
wt%	(a)	(b)	(m)	(a)	(b)	(m)	(a)	(b)	
SiO_2	69.42	70.03	71.82	62.88	65.31	72.53	57.32	58.08	71.78
TiO_2	0.47	0.36	0.00	0.81	0.62	0.00	0.97	0.92	0.00
Al_2O_3	17.39	16.65	14.53	20.70	18.86	13.39	22.60	22.17	13.82
FeO	4.10	3.05	0.00	5.86	4.38	0.00	7.98	7.59	0.00
MnO	0.01	0.01	0.00	0.00	0.00	0.00	0.00	0.00	0.00
MgO	1.74	1.29	0.00	2.21	1.64	0.00	3.55	3.56	0.00
CaO	1.10	0.92	0.39	0.22	0.28	0.37	1.15	1.10	0.15
Na_2O	1.61	1.89	2.71	0.62	1.03	2.11	2.39	2.20	3.34
K_2O	3.60	4.19	5.89	5.92	5.91	6.15	2.89	3.00	5.20
H_2O	0.56	1.61	4.66	0.76	1.98	5.45	1.15	1.38	5.72
T(°C)			810			750			750
P (kbar)			5.1			3.8			4.2
mol%			0.38			0.4			0.06